HIROSHIMA UNIVERSITY

DOCTORAL THESIS

Near-infrared observational studies of black hole low mass X-ray binary GRS 1915+105 in the X-ray low luminous state

Author:
Fumiya IMAZATO

Supervisor:
Dr. Yasushi FUKAZAWA

February 21, 2022

HIROSHIMA UNIVERSITY

Abstract

Physical Sciences

Doctor of Science

Near-infrared observational studies of black hole low mass X-ray binary GRS 1915+105 in the X-ray low luminous state

by Fumiya IMAZATO

A black hole low-mass X-ray binary is a binary system of a black hole and a low mass star (less than solar mass, hereafter companion star). The black hole is surrounded by an accretion disk and occasionally ejects plasma with relativistic velocity (jet). The energy of the object is supplied by the gravitational energy released by the gas from the companion star as it falls into the black hole. The radio and soft X-ray emissions are synchrotron radiation from the jet and blackbody radiation from the inner parts of the disk, respectively. Candidate for the origin of the near-infrared (NIR) emission is the jet, the outer parts of the disk and the companion star. Which of these is the main origin depends on the state of the object. The main origin can be determined by detailed NIR observations and multi-wavelength observations with the radio and X-ray bands. If the origin of the NIR emission can be accurately determined, more detailed information on the geometry and emission mechanisms of the jet and the disk can be provided from multi-wavelength spectral analysis.

The black hole low-mass X-ray binary GRS 1915+105 is a well-known source; the first observation of superluminal motion of radio blobs in our galaxy, 14 regular patterns of X-ray variation, and relationship between a disk wind and the jet. One of the other most unique characteristics, not seen in any other black hole low-mass X-ray binary, is that GRS 1915+105 has continuously been in the high flux state in the X-ray band for about 26 years since its discovery in 1992. The radio is also bright, often in the range of a few mJy to several hundred mJy, leading to many opportunities for the multi-wavelength observation between the radio and X-ray bands. NIR observations were also performed, but were much smaller in amount than the radio and X-ray observations.

In mid-2018 and mid-2019, GRS 1915+105 suddenly dimmed and transitioned to the faintest state in soft X-ray observations ($<$10 keV). From the X-ray spectral analysis, the main factor of the second X-ray dimming was found to be the X-ray obscuration. However, there are few reports of the NIR observations before and after the second dimming, and the characteristics of the NIR flux variations and the origin of the NIR emission are not clearly understood.

We performed long-term, dense NIR observations in two bands with Kanata telescope at the Higashi-Hiroshima Observatory from April 2019 to November 2020. The radio and X-ray data were taken from Yamaguchi interferometer and from MAXI and RXTE, respectively.

Focusing on the variation timescales longer than one day, the followings were found. Comparing with the NIR flux until 2008, the NIR flux after the second X-ray dimming was found to be higher than the maximum flux level of the past. A more detailed investigation of the NIR variation before and after the second X-ray dimming showed that there was a NIR brightening during the X-ray dimming. The radio flux was higher after the second X-ray dimming as well as the NIR flux.

Focusing on the variation timescales shorter than one day, the followings were found. After the second X-ray dimming, the NIR flux showed variations on timescales of more than ten minutes (flares). However, the flare was not seen on all days, and on some days flare was absent during more than 5 hours of observations. The base line flux of the flare after the second X-ray dimming was clearly higher than that of the past flares. On the other hand, there was no obvious difference of the rise and decay timescales and amplitude of the flare.

Before and after the second X-ray dimming, the followings were found for the origin of the NIR emission of the variation timescales longer than one day. Before the second X-ray dimming, and the radio to NIR spectrum could not be explained by the jet. This suggests that the origin of the NIR emission before the second X-ray dimming is not the jet but the disk or the companion star. On the other hand, after

the second X-ray dimming, the radio and NIR fluxes were both high, and the high fluxes were kept for at least 95 days in both bands. This suggests that the jet is the main origin of the NIR emission after the second X-ray dimming. However, since the NIR flux was higher than the maximum flux level of the past, non-jet origin may also contribute to the NIR band. The non-jet candidate is not the disk due to the low X-ray flux, but the X-ray obscuration.

After the second X-ray dimming, the followings were found for the variation on timescales of shorter than one day. There are two scenarios that explain the difference of the base line flux of the past and after the X-ray dimming. The first is that the intrinsic rise and decay timescales are different and the flare after the X-ray dimming has longer intrinsic timescales. The second is that the origin of the flare after the second X-ray dimming is different from the past flare, and that the origin of the flare after the second X-ray dimming is the jet and the non-jet origin with longer timescales.

Contents

List of Figures

List of Tables

Chapter 1

Introduction

1.1 About black hole X-ray binaries

The cartoon of the black hole low mass X-ray binary is shown in Figure 1.1. The black hole low mass X-ray binary is a binary system of a low mass star (less than solar mass, hereafter companion star) and a black hole. The matter of the companion star moves into the black hole. This is attributed to the roche lobe overflow caused by shape of the gravitational potential formed in the binary system as shown in Figure 1.2. Due to the gas has angular momentum, it does not fall directly into the black hole, but forms a disk around the black hole (hereafter accretion disk). In the accretion disk, the gas transfers its angular momentum to the outer gas due to its viscosity, and the disk diffuses as shown in Figure 1.3. Some black hole low mass X-ray binaries eject plasma with relativistic velocity (hereafter jet).

1.1.1 Accretion disk

As the matter falls into the inner part of the disk (toward the black hole) due to the viscosity, it gradually releases its energy, and the local disk has a higher temperature. This is because the gravitational potential for the matter follows the form of r^{-1} except in the vicinity of a black hole, where r is the distance from the matter to the black hole, and the matter releases more energy as falling inward.

If thermal energy resulting from the release of the gravitational energy is completely converted to radiation energy, the accretion disk is optically-thick and geometrically-thin, called a standard disk (Shakura and Sunyaev, 1973). The standard disk has a spectrum of superimposed blackbody radiation depending on the temperature at each radius of the disk, as shown in Figure 1.4.

If the accretion disk is hot and its density is low, radiative cooling is ineffective and advection is dominant. The accretion disk is called an advection dominated accretion flow (ADAF) (Ichimaru, 1977; Narayan and Yi, 1994). Because of the high temperature, the accretion disk expands vertically compared to the standard disk. The main radiations of ADAF are thermal bremsstrahlung, synchrotron radiation, and radiation of the inverse Compton scattering.

When the density of the accretion disk becomes high, the optical thickness of the disk becomes high, and the matter falls into the black hole before the photon reaches the disk surface. The phenomenon is called photon supplementation, and the radiative cooling is lower than that of the standard disk. Such an accretion disk is called a slim disk (Abramowicz et al., 1988).

As the density of the accretion disk increases, the radiative energy also increases, and the luminosity of the disk becomes higher. However, the luminosity has a limit, which is the highest when gravity and radiation pressure are balanced. This luminosity is called Eddington luminosity denoted as L_{Edd}. The luminosity of the disk, L,

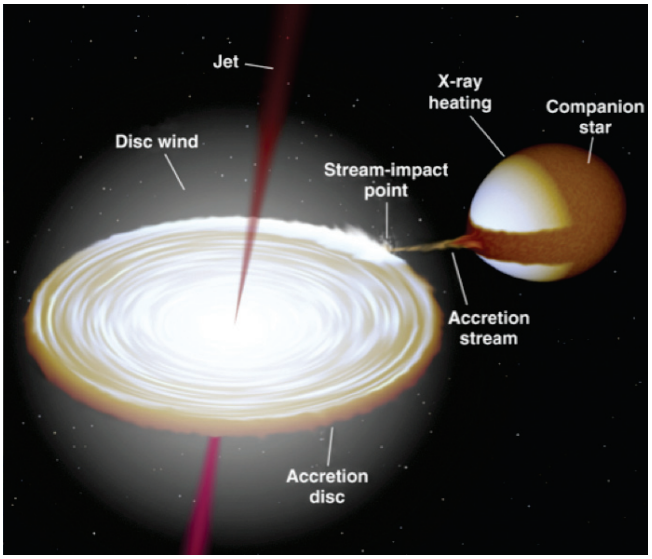

FIGURE 1.1: Sketch of the black hole low mass X-ray binaries. From Fender and Belloni (2012).

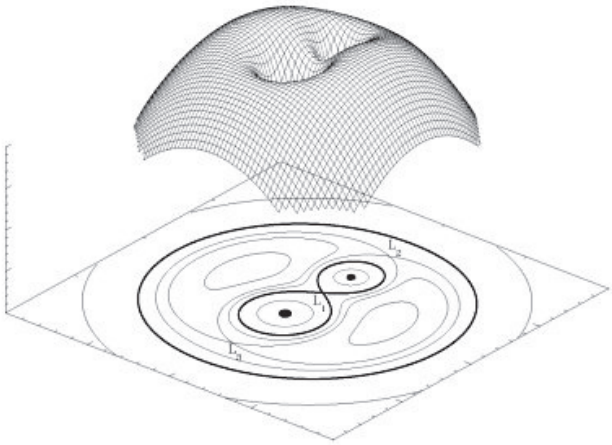

FIGURE 1.2: Gravitational potential of a binary system in three dimensions. From http://hemel.waarnemen.com/Informatie/Sterren/samenvatting_proefschrift.html

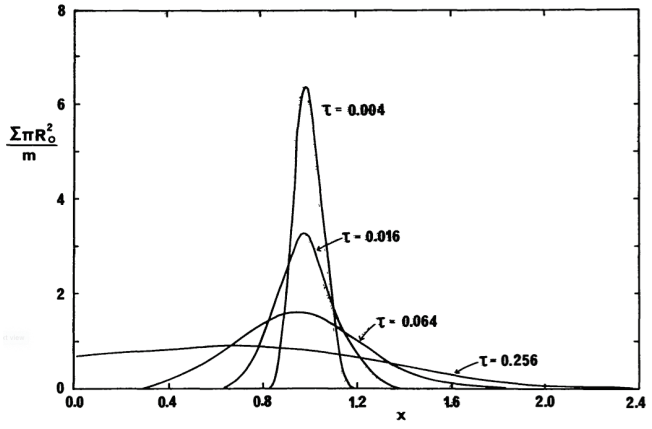

FIGURE 1.3: An accretion disk expanding due to viscosity. From Pringle (1981).

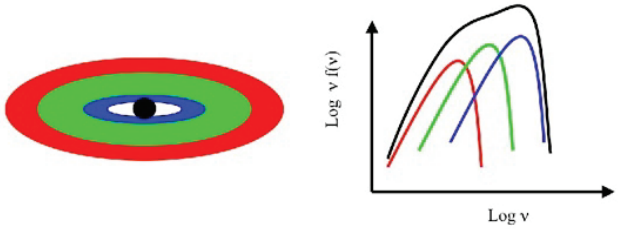

FIGURE 1.4: Sketch of the spectrum of standard disk. The left picture shows a black hole (black) and accretion disk (red, green, and blue), and the temperature of the accretion disk is higher toward the inner part. The right picture shows the spectrum of the standard disk in black. The horizontal and vertical axes are the frequency and the brightness at each frequency, respectively. The spectrum of the standard disk is a superposition of the blackbody radiation of each color shown on the left picture. From https://sites.ualberta.ca/~jgladsto/Site/accretion.html.

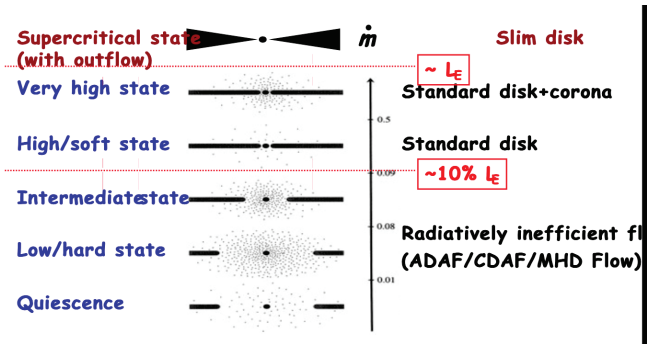

FIGURE 1.5: Illustration for three model of the accretion disk and $\dot{m}$. The vertical axis is the accretion rate $\dot{m}$ or luminosity L. The appropriate model of the accretion disk is a standard disk for the accretion rates of roughly several tens of percent, the slim disk for higher accretion rates, and the ADAF for accretion rates of a few percent or less. From https://slideplayer.com/slide/4561569/, the original image is from Esin, McClintock, and Narayan (1997).

divided by L_{Edd}, is called Eddington fraction which expresses how many matters in the accretion disk are falling into the black hole. In the same sense as the Eddington fraction, the accreting mass per unit time $\dot{m}$ is a parameter of disk models. The relationship between the mass accretion rate $\dot{m}$ and the accretion disk models is shown in Figure 1.5.

At the outer disk, warmed by radiation from the inner parts of the disk, matter moves vertically away from the disk surface, exceeding the escape velocity (Begelman, McKee, and Shields, 1983). Due to the radiation pressure from the inner parts of the disk, disk wind is launched as shown in Figure 1.6. In addition to thermally driven mechanism (described above), there are two other possible mechanisms for driving the disk wind: magnetically driven (Proga, 2003; Miller et al., 2008) and line-force driven (Cordova and Mason, 1982). When there is a disk wind between the observer and the radiation region, absorption lines are observed in the X-ray spectrum, as shown in Figure 1.7.

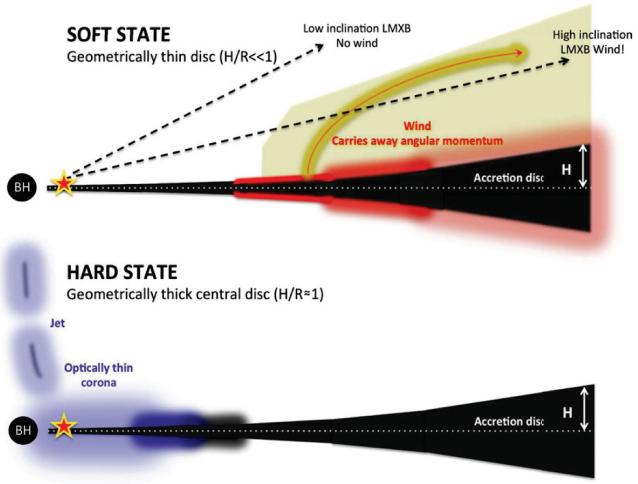

FIGURE 1.6: Sketch of the disk wind. The upper and lower panels show the case with and without disk wind, respectively. The black circle with white letters "BH" is the black hole, and the black object to its right is the accretion disk. In the upper panel, the red color represents the accretion disk warmed by X-rays, and the yellow color represents the disk wind. From Ponti et al. (2012).

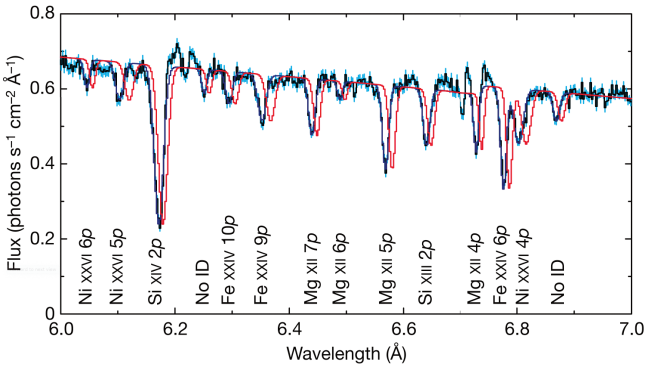

FIGURE 1.7: An example of X-ray spectrum with absorption lines due to disk wind. The horizontal and vertical axes are the wavelength and flux, respectively. The black, light blue, and red colors are the observed data, error bars, and expected absorption lines for a rest system, respectively. The texts at the bottom represent the name of the atom corresponding to each absorption line. From Miller et al. (2006).

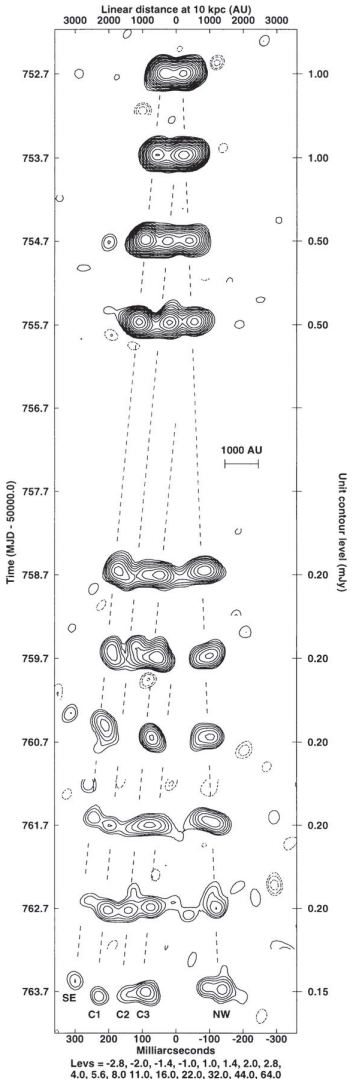

FIGURE 1.8: Radio jets of X-ray binary observed for about 10 days. From Fender et al. (1999).

1.1.2 Jet

Jets from X-ray binaries have been confirmed by radio observations as shown in Figure 1.8. The jet radiation is known to be synchrotron radiation in radio and NIR bands based on spectral and polarization studies (e.g., Fender 2006; Russell 2018).

An illustration of the jet spectrum is shown in Figure 1.9. The intensity of the synchrotron radiation from various positions from the inner jet gradually decreases due to adiabatic expansion and other factors, but the radiation area increases. As a result, the spectrum mainly consists of two parts, one with a spectral index[1] of $\sim$0 (flat) and the other with a spectral index of $\sim$-0.6 (steep) (e.g., Markoff, Falcke, and Fender 2001; Heinz and Sunyaev 2003). The frequency that the spectral index changes is called a break frequency, and the optical thickness of jets becomes thick below this frequency. The jet model assumes that the shape of the jet is conical, the bulk Lorentz factor is constant, and the magnetic field strength and electron energy distribution in the jet are power-law (Blandford and Königl, 1979).

[1]The spectral index α is the value of power when the flux is expressed by the power-law formula of frequency.

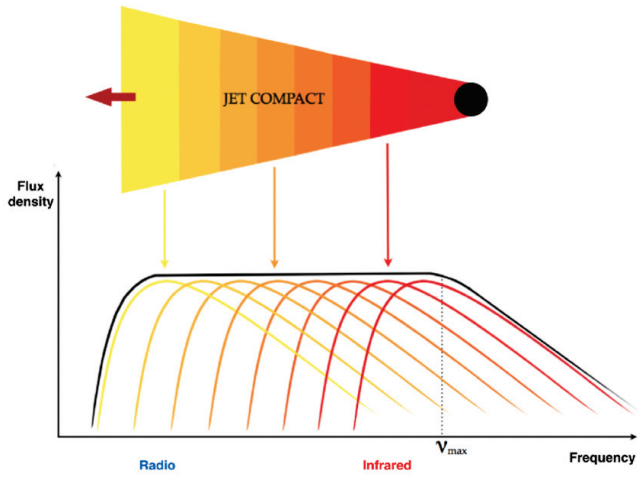

FIGURE 1.9: Illustration of the jet and its spectrum of X-ray binary. From *High Time-Resolution Astrophysics* (2018)

1.2 State transition of black hole X-ray binaries

Black hole low mass X-ray binaries brighten rapidly in X-ray band roughly every a few years, it is called outburst. Example of the outburst of frequently observed black hole low mass X-ray binaries are shown in Figure 1.10. In the outburst, a characteristic phenomenon of X-ray binary occurs: state transition.

During the state transition, not only the luminosity but also the shape of the X-ray spectrum changes. Figure 1.11 shows the luminosity and the spectral shape of GX 339-4, a famous black hole low mass X-ray binary, during multiple state transitions. At beginning of the state transition, the black hole low mass X-ray binaries are located in the lower-right of the figure. As it brightens, it moves from the lower-right to the upper-right in the figure. When the brightness reaches its peak, it moves from the upper-right to the upper-left in the figure. The shift from right to left means change of the spectral shape. Concretely, it means that the fraction of high-energy photons decreases and the fraction of low-energy photons increases. After the source becomes fainter (upper-left to lower-left), the spectral shape returns to its original shape (lower-left to lower-right). The sequence of changes in luminosity and spectral shape occurs in a single state transition. The lower-right and upper-left states of the X-ray binary are called low/hard state and high/soft state, respectively. The state between these two states is called intermediate state.

Based on the X-ray spectral and temporal analysis, the cause of the state transition is thought to be the change of physical properties of the accretion disk. Figure 1.5 shows how accretion disk changes by state. In the low/hard and high/soft states where the accretion rate is low, the inner region becomes the ADAF and the outer region becomes the standard disk (section 1.1.1).

During the state transition, the flux of the jet changes as well as that of the accretion disk. Figure 1.12 shows the radio flux (green plot) in the soft state and hard state. In the soft state, the jet radiation is not detected. On the other hand, in the hard state, the jet radiation is detected and the flux is higher than the upper limit of the soft state. The jet in the soft state is considered to be absent or too faint to be detected (e.g., Fender, Belloni, and Gallo 2004; Drappeau et al. 2017).

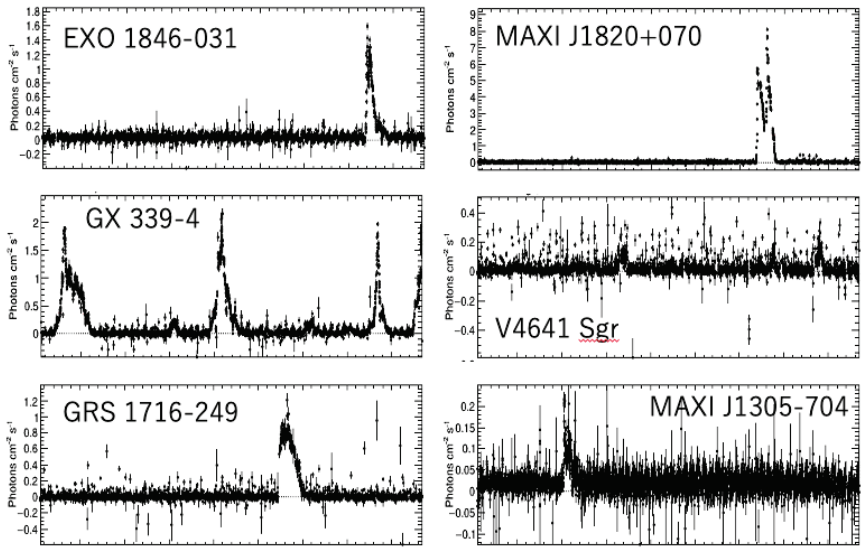

FIGURE 1.10: Example of X-ray lightcurves for the black hole low mass X-ray binary. The letters in each figure represent the object names. The horizontal axis represents about 10 years of time. These figures are obtained from MAXI web page (`http://maxi.riken.jp/top/lc.html`).

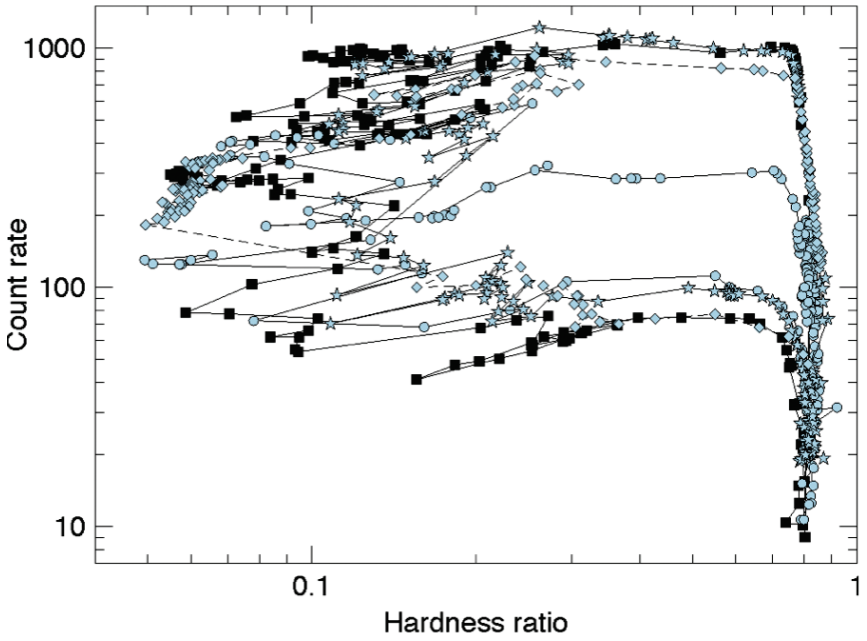

FIGURE 1.11: Hardness Intensity diagram for GX 339-4 in 2002 and 2003. The vertical and horizontal axes represent the luminosity and the spectrum shape, respectively. From *High Time-Resolution Astrophysics* (2018).

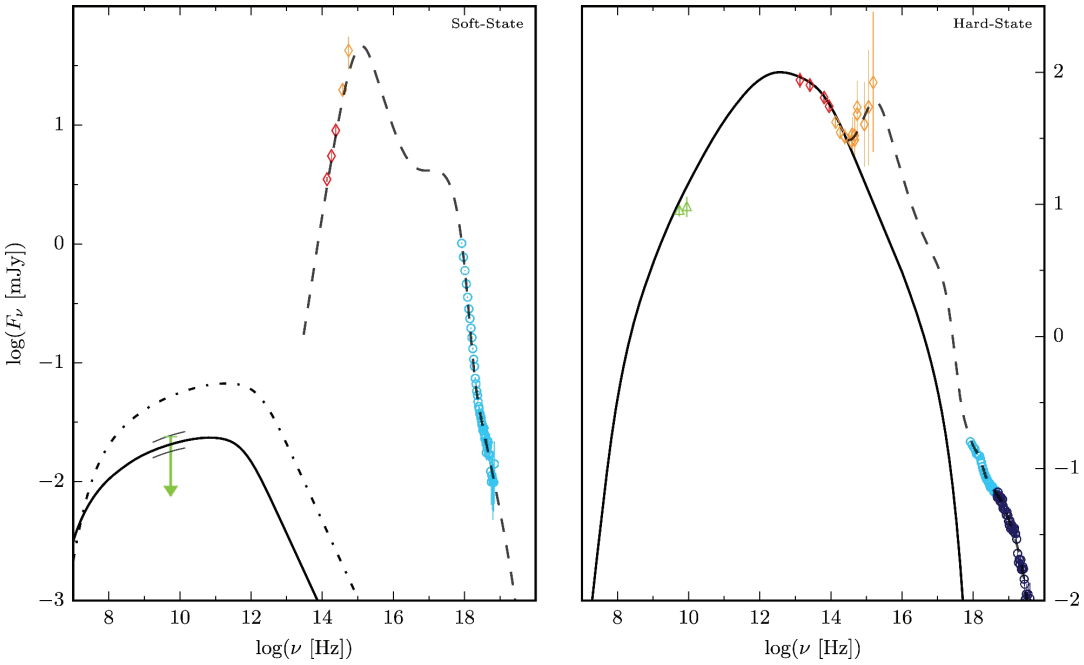

FIGURE 1.12: Multi-wavelengths spectra of the black-hole X-ray binary GX 339-4 in the soft state (left panel) and hard state (right panel) during 2010 outburst. Green is the radio data, and the radio plot in the left panel shows 3 σ upper limit of the flux. From Drappeau et al. (2017).

1.3 GRS 1915+105

GRS 1915+105 has been the brightest black hole low mass X-ray binary since the discovery of GRS 1915+105 in 1992 (Castro-Tirado, Brandt, and Lund, 1992). It consists of $12.4^{+2.0}_{-1.8}$ $M_\odot$ black hole (Reid et al., 2014) and K5 III companion star (Ziółkowski and Zdziarski, 2017). Orbital period is 33.85 $\pm$ 0.16 days (Steeghs et al., 2013), and the distance is $8.6^{+2.0}_{-1.6}$ kpc (Reid et al., 2014). This is also a prototypical microquasar; superluminal motion of radio blobs was observed, indication the existence of the relativistic jet. So far, many observations have been performed at multi-wavelengths. The following three subsections (1.3.1, 1.3.2, and 1.3.3) we describe the important results from the past observations.

1.3.1 X-ray observations

One of the unique features of GRS 1915+105 is that there are over 14 regular patterns of variation in the X-ray lightcurve (Belloni et al., 2000; Klein-Wolt et al., 2002; Hannikainen et al., 2005). These variation patterns are classified based on the appearance of the X-ray lightcurve and spectrum. Figure 1.13 shows the variation of X-ray flux for several patterns. The data in the figure is from the Rossi X-ray Timing Explorer (RXTE) (Bradt, Rothschild, and Swank, 1993) satellite from January 1996 to December 1997. The X-ray lightcurve of the RXTE satellite covers the energy range of 2-60 keV. The vertical axis (HR1) and horizontal axis (HR2) in the upper panel of the figure are defined as follows: HR1=B/A, HR2=C/A. The A, B, and C are photon counts in the 2-5, 5-13, and 13-60 keV, respectively.

Belloni et al. (2000) focused on the HR1-HR2 diagram for all classes of the regular variation pattern in GRS 1915+105 and found that there are three main states: A, B,

and C. Figure 1.14 shows the three states and the directions of their transitions in the HR1-HR2 diagram. Belloni et al. (2000) defined the three states as follows:
"

- A: low count rate, low HR1 and HR2;
- B: high count rate, high HR1;
- C: low count rate, variable HR2 depending on the length of the event

"
They proposed that the variation pattern of the X-ray lightcurve can be explained by the combination of these three states. For example, the class λ, the states are a combination of a B-C-A-B-C-A-B.... and so on.

The three phenomenologically classified states have physical interpretations. Belloni et al. (1997) analyzed the X-ray spectra of states B and C with a "standard" model (Mitsuda et al., 1984), and found that the standard disk and a power-law component are dominant in states B and C, respectively. They also analyzed the spectrum of state A and found that the temperature of the accretion disk is lower than that of state B. A summary of the physical interpretation of these three states is as follows (the statement is cited from Fender and Belloni, 2004 and the physical interpretations were modified to be highlighted in bold text).
"

- State A: softer spectrum, **dominated by a disc component with** $kT_{in} > 1keV$. Mostly little time variability.
- State B: softer spectrum, **dominated by a disc component with a larger temperature than state A**. Substantial red-noise variability on timescales $>$ 1s.
- State C: hard colors, with the spectrum **dominated by a relatively flat power-law (**$\Gamma = 1.8 - 2.5$**)**. White noise variability on timescales $>$ 1s.

"
Where k is the Boltzmann constant, T_{in} is the temperature of the accretion disk, and Γ is the photon index.

1.3.2 Radio observations

The radio jets of GRS 1915+105 are of two types: large superluminal jet, steady jet (Yadav, 2006). The superluminal jet that exhibits superluminal motion is a phenomenon in which apparent velocity of the jet exceeds the speed of light. This occurs when the speed of radio source approaching to the observer is close to the speed of light (Rees, 1966). Figure 1.15 shows a superluminal jet of GRS 1915+105, the first source discovered in our galaxy (Mirabel and Rodríguez, 1994). The radio flux of the superluminal jet is up to $\sim$ 300–600 mJy (e.g., Klein-Wolt et al. 2002), and the radio spectrum shows an optically thin feature (e.g., Foster et al. 1996).

GRS 1915+105 almost always shows the steady jet as shown in Figure 1.17. In the figure, the superluminal jet appears roughly at Day 0, and the steady jet appears for $\sim$20 days (Day -20 – 0). The steady jet ($<$200 AU) is smaller than the superluminal jet and is also called a compact jet, as shown in Figure 1.16. The radio flux of the steady jet is up to $\sim$ 100 mJy (e.g., Klein-Wolt et al. 2002), and the radio spectrum shows an optically thick feature ($\alpha \sim 0$) (e.g., Dhawan, Mirabel, and Rodríguez 2000; Fuchs, Mirabel, and Claret 2003).

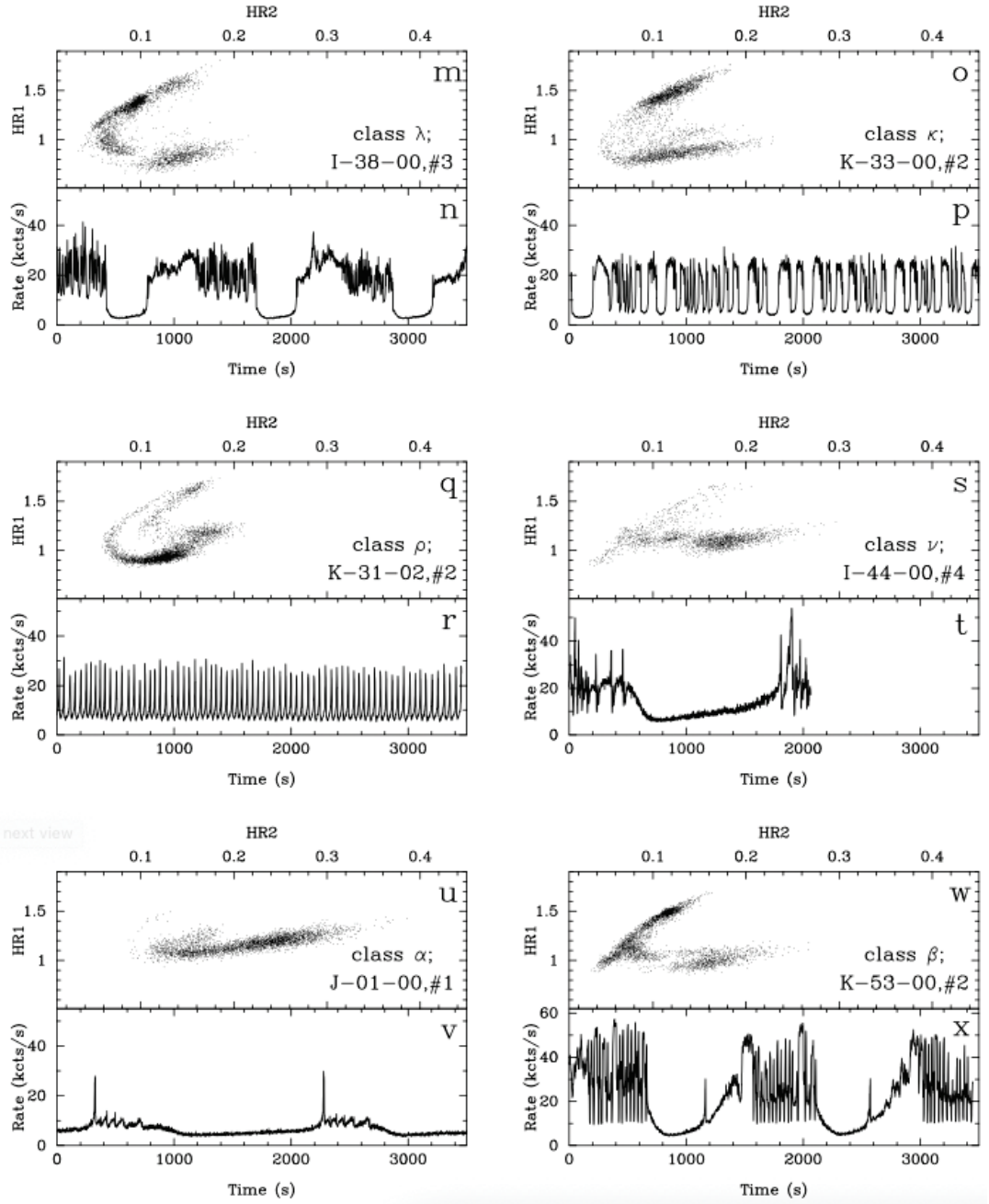

FIGURE 1.13: Examples of the X-ray lightcurves (panels n, p, r, t, v, and x) and the spectral information (panels m, o, q, s, u, and w) for the 6 variation patterns of GRS 1915+105. The definitions of vertical axis (HR1) and horizontal axis (HR2) of the upper panel are described in the text. From Belloni et al. (2000).

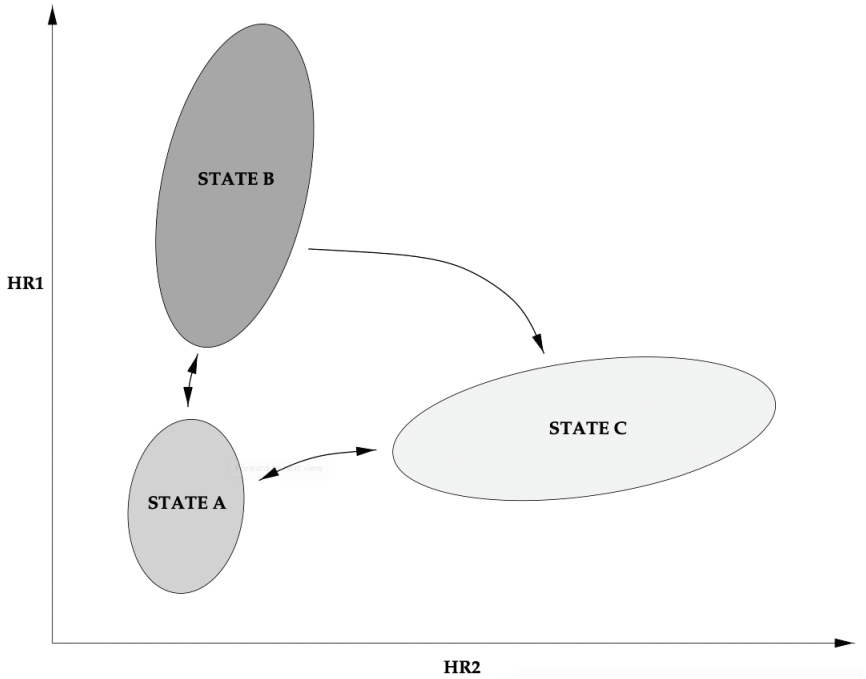

FIGURE 1.14: Three main states in HR1-HR2 diagram. The arrows represent the direction of the observed state transitions. From Belloni et al. (2000).

The relationship between the steady jet and the superluminal jet can be explained by the scenario of Vadawale et al. (2003) as shown in Figure 1.18. They found the absence of the Compton cloud after the onset of the superluminal jet from temporal analysis and variation of hard X-ray flux. The absence can be interpreted in the way that a part of the Compton cloud was ejected as the jet. If a part of the Compton cloud is ejected with a high velocity when a continuous jet (steady jet) with a low velocity already exists, particle acceleration due to internal shock occurs, and radio emission becomes bright (superluminal jet). This scenario can explain the appearance of the superluminal jet after the steady jet, and the difference in flux and spectrum between them.

1.3.3 NIR observations

GRS 1915+105 shows flux variability in the NIR band on timescales ranging from minutes to months. Figure 1.19 shows examples of light curves with variation timescales of minutes and months (Neil, Bailyn, and Cobb, 2007; Eikenberry et al., 2008). In the following, we present the results of NIR observations, focusing on short-term (less than one day) and long-term (more than one day).

The NIR origin of the short-term component for GRS 1915+105 is considered to be jet. Eikenberry et al. (1998) performed simultaneous observations of X-ray and NIR bands, and found that the time-lag between the X-ray and NIR flares was $\sim$300 seconds and the X-ray and NIR variations were decoupled in the later phase of the flares, as shown in Figure 1.20. Based on their results, they concluded that the NIR main origin of the short-term component is not the accretion disk. Mirabel et al. (1998) performed simultaneous observations of radio, NIR, and X-ray bands, and succeeded in explaining the time-lag of the peak flux epochs between NIR and radio bands with the adiabatically expanding cloud model of the jet (van der Laan, 1966).

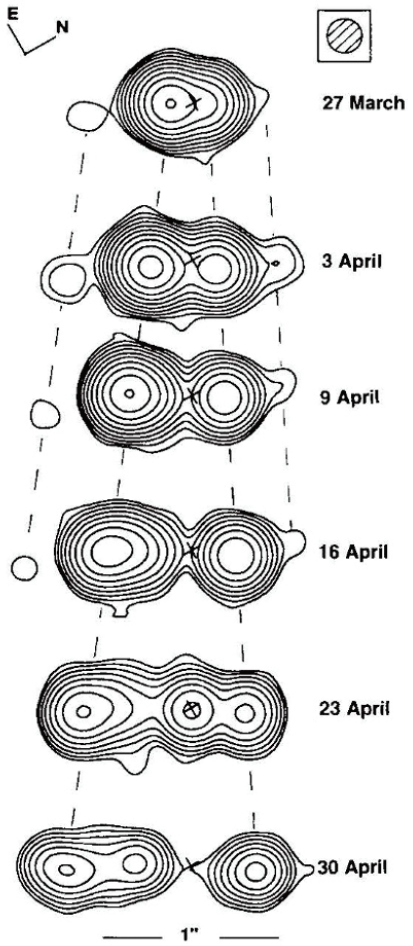

FIGURE 1.15: Radio blob image of GRS 1915+105 showing superluminal motion. The apparent velocities β_{app} of the two blobs are 1.25±0.15 and 0.65±0.08, while the true velocity β_{true} is 0.92±0.08. The contour lines indicate the radio intensity, and the crosses indicate the same position on the sky. From Mirabel and Rodríguez (1994).

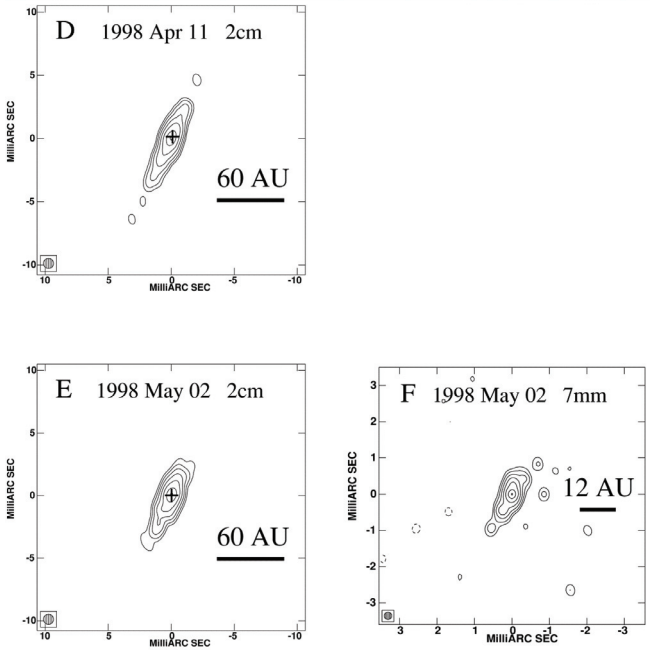

FIGURE 1.16: Radio image of the compact jet of GRS 1915+105 in April and May 1998. The black horizontal bar in each figure represents the spatial scale of the magnitude of the number above it. From Dhawan, Mirabel, and Rodríguez (2000).

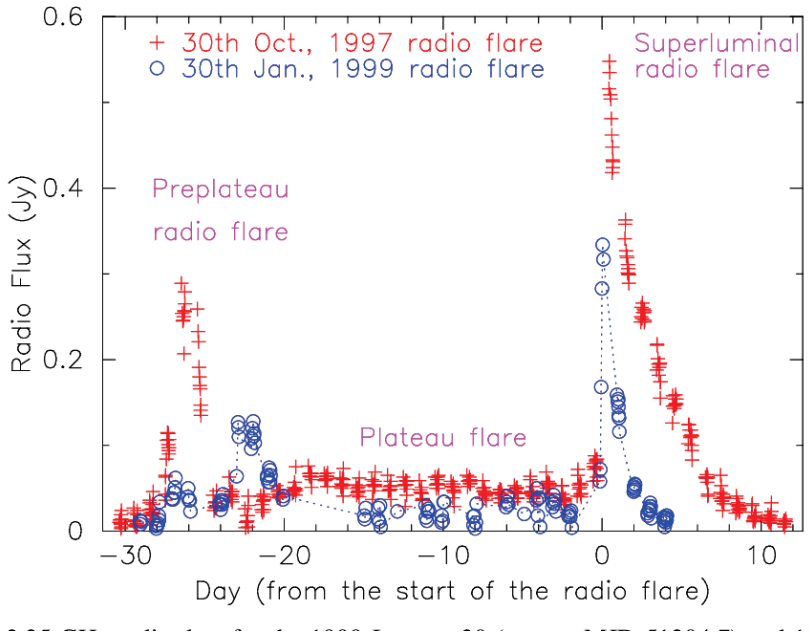

FIGURE 1.17: Radio light curves of GRS 1915+105 ejecting superluminal jets. Day 0 on the horizontal axis is the start time of the superluminal flare. The red and blue plots are the light curves in October 1997 and January 1999, respectively. From Yadav (2006).

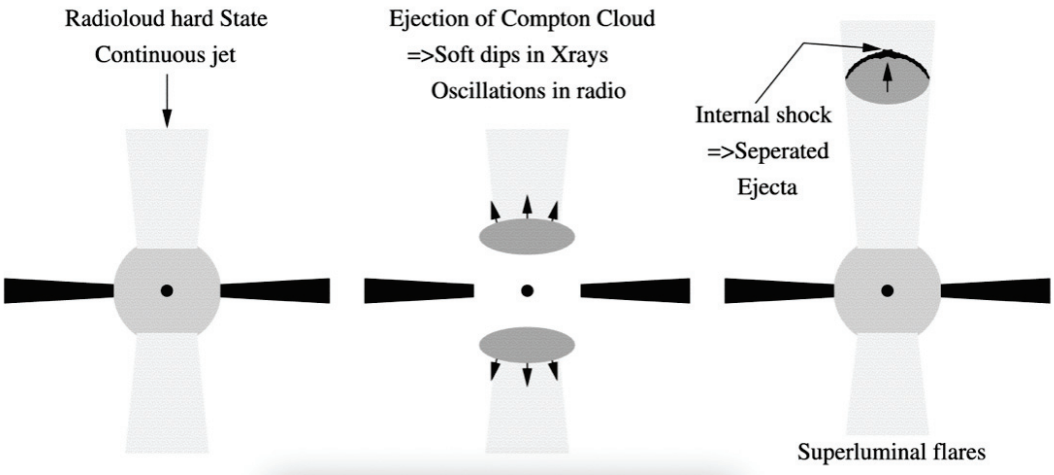

FIGURE 1.18: Illustration of jet events in GRS 1915+105. Continuous jet corresponds to the compact jet in the text, and "Superluminal flares" corresponds to the superluminal jet. From bottom panel of Figure 10 in Vadawale et al. (2003).

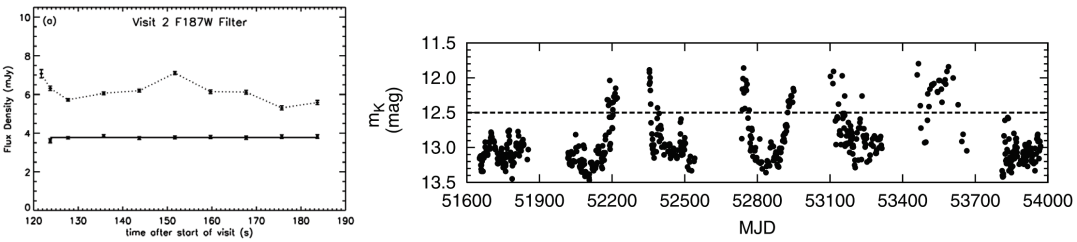

FIGURE 1.19: Examples of variability of NIR flux of GRS 1915+105 on timescales of minutes (left panel) and months (right panel). The units of the horizontal axis in the left and right panels are second and day, respectively. In left panel, the plot with dotted lines corresponds to GRS 1915+105 and the plot with solid lines to the reference star. The left and right panels are from Eikenberry et al. (2008) and Neil, Bailyn, and Cobb (2007), respectively.

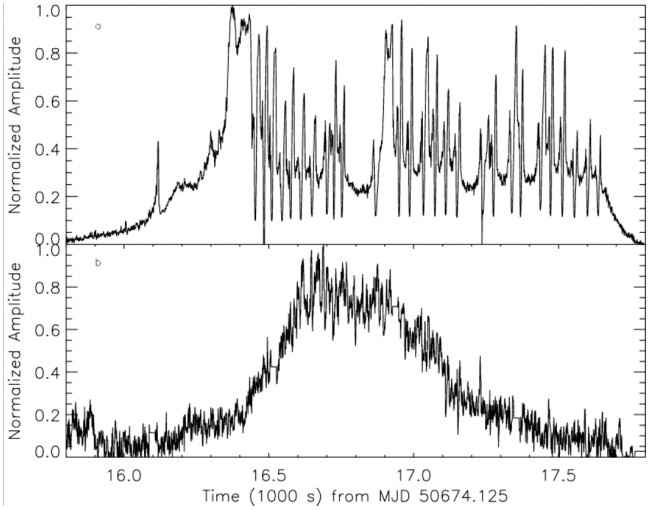

FIGURE 1.20: Simultaneous light curves of X-ray (top panel) and NIR (bottom panel) bands of GRS 1915+105. The X-ray oscillation continues even though the NIR flux decreases in the later phase of the flares around 17.0–17.5 on the horizontal axis. From Eikenberry et al. (1998).

Fender and Pooley (2000) also performed simultaneous radio and NIR observations, and reported the NIR variations synchronized with radio variations (Figure 1.22), suggesting that the NIR origin of the short-term component is jet.

The NIR origin of the long-term component for GRS 1915+105 is unclear to date. Neil, Bailyn, and Cobb (2007) found that there are possibly several NIR origins from the correlation between NIR flux and X-ray hardness ratio (Figure 1.23), since in not all of them NIR correlate with the X-ray hardness ratio. They suggested that the NIR component with low flux is a thermal emission (e.g., from the accretion disk) and the NIR component with high flux is possibly a non-thermal emission. Arai et al. (2009) found anticorrelated variation between the NIR flux and the radio and X-ray fluxes in 2007–2008 as shown in Figure 1.24. They concluded that the NIR origin of the long-term component is not jet, based on the anti-correlation between NIR and radio fluxes. In addition, the timescale of the flux variation and the lack of orbital period variations ruled out companion star origin. From these discussions they suggested that the accretion disk is possibly the origin of the NIR emission, but the scenario cannot explain the anti-correlation between X-ray and NIR fluxes. In contrast to the short-term observations, data of the long-term observation is still insufficient for the

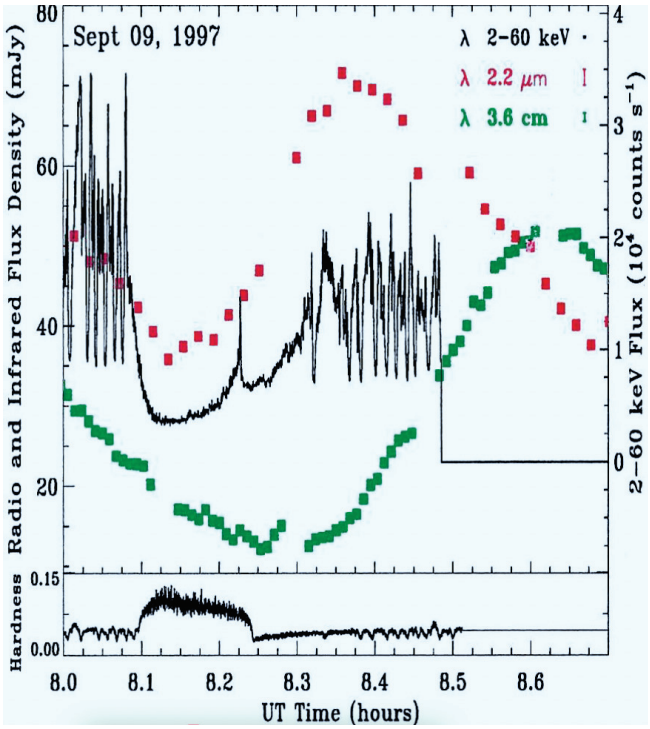

FIGURE 1.21: Simultaneous light curves of radio (green), NIR (red) and X-ray (black) bands of GRS 1915+105 on September 9, 1997. The left and right sides of the vertical axis are the radio and NIR fluxes and the X-ray flux, respectively. From Mirabel et al. (1998).

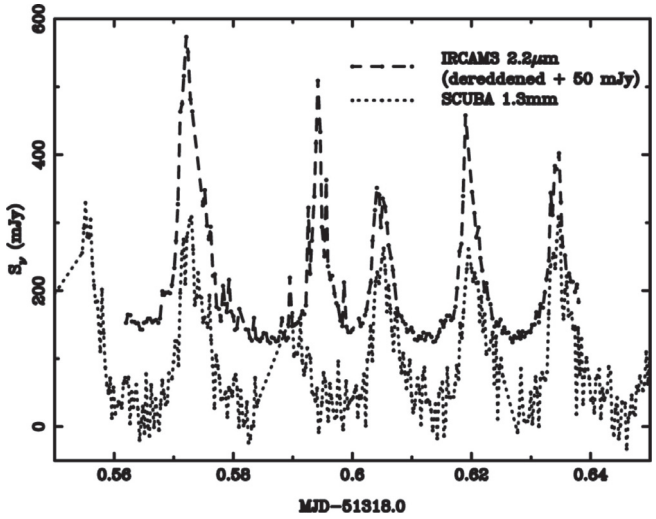

FIGURE 1.22: Simultaneous light curves of radio (dot) and NIR (dash-dot line) bands of GRS 1915+105 on May 20, 1999. From Fender and Pooley (2000).

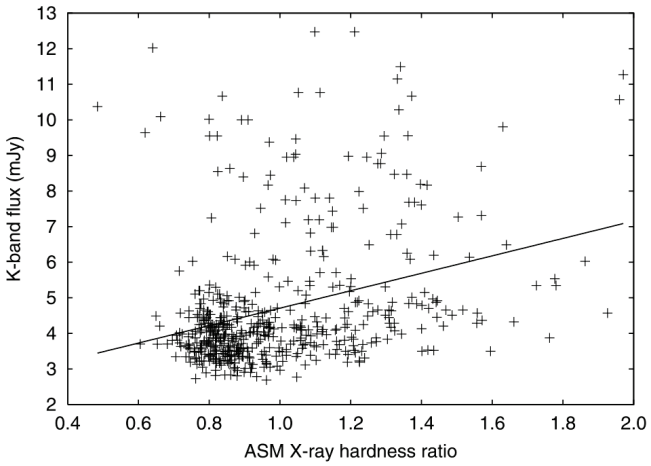

FIGURE 1.23: Correlation between NIR flux (vertical axis) and X-ray hardness ratio (horizontal axis) over 7 years. The data points are taken from the light curve in left panel of Figure 1.19. The solid line is the best linear function fitted with the least squares method, and the correlation efficient is 0.330. From Neil, Bailyn, and Cobb (2007).

purpose of understanding the NIR origin of the long-term component, and dense monitoring with radio, NIR, and X-ray bands is needed.

1.3.4 Sudden changes in X-ray band in 2018 and 2019

Unlike other low-mass X-ray binary stars, GRS 1915+105 has continuously been in the high-flux state for about 26 years since it was discovered the year 1992 (Castro-Tirado, Brandt, and Lund, 1992). However, soft X-ray (<10 keV) flux of GRS 1915+105 suddenly decreased in the middle of 2018. And GRS 1915+105 became the lowest flux state in the soft X-ray observations by The Rossi X-ray Timing Explorer (RXTE) and The Monitor of All-sky X-ray Image (MAXI) (Negoro et al., 2018). Furthermore, the X-ray flux became one order of magnitude lower from April to May 2019 (Homan et al., 2019) and then the low-flux state continues for about a year. Figure 1.25 shows the X-ray light curve of GRS 1915+105 including the two X-ray dimming features.

The X-ray dimming implies that the outburst of about 26 years ended and GRS 1915+105 seemed to become quiescence state like other low mass X-ray binaries. However, Motta et al. (2021) found bright radio emission of about 100 mJy in their radio observations during the period (top panel of Figure 1.25). This indicates that GRS 1915+105 has not transitioned to the quiescent state.

Based on the X-ray analysis with the model of the X-ray obscuration, Balakrishnan et al. (2021) found that the Eddington luminosity ratio with correction for the obscuration was $\sim$20% and the hydrogen column density of the obscuration was $\sim 10^{23}$ cm^{-2} before the second X-ray dimming. They also found that the Eddington luminosity ratio did not change significantly before and after the second dimming, but the hydrogen column density of the obscuration increased by about an order of magnitude, as shown in Figure 1.26. These results mean that the X-ray obscuration is the main factor for the second dimming.

After the second X-ray dimming, high NIR flux was reported (Imazato et al., 2019; Murata et al., 2019; Vishal, Banerjee, and Dipankar, 2019). However, due to the small number of observations, the characteristics of the variation and the origin of the NIR emission has been not clearly understood after the second dimming. In

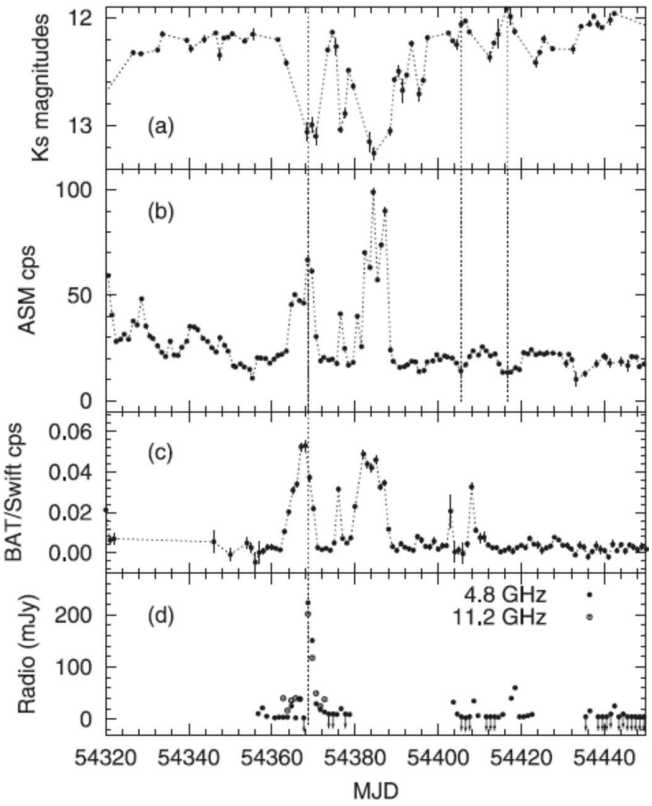

FIGURE 1.24: Multi-wavelengths light curves of NIR, soft X-ray, hard X-ray and radio bands, from top to bottom of GRS 1915+105 in 2007–2008. The three vertical dashed lines represent the anti-correlation of the NIR and X-ray fluxes. From Arai et al. (2009).

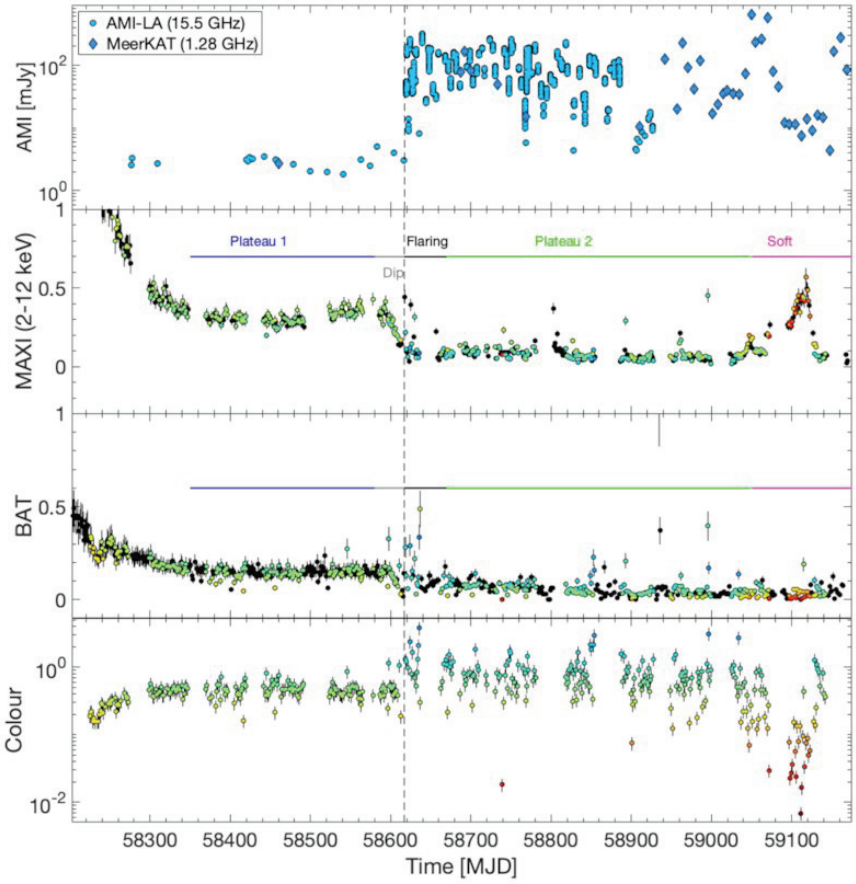

FIGURE 1.25: Multi-wavelength light curves for radio and X-ray bands in 2018 – 2019. From the top panel, radio flux, soft X-ray flux, hard X-ray flux, and X-ray colour are shown. The color of the plot in each panel of X-ray data corresponds to the X-ray colour in the bottom panel. The first decrease of the soft X-ray flux in 2018-2019 is up to MJD∼58300 and the second is up to MJD∼58600. From Motta et al. (2021).

addition, there are no reports of the NIR emission before the second dimming, except for the data in this paper.

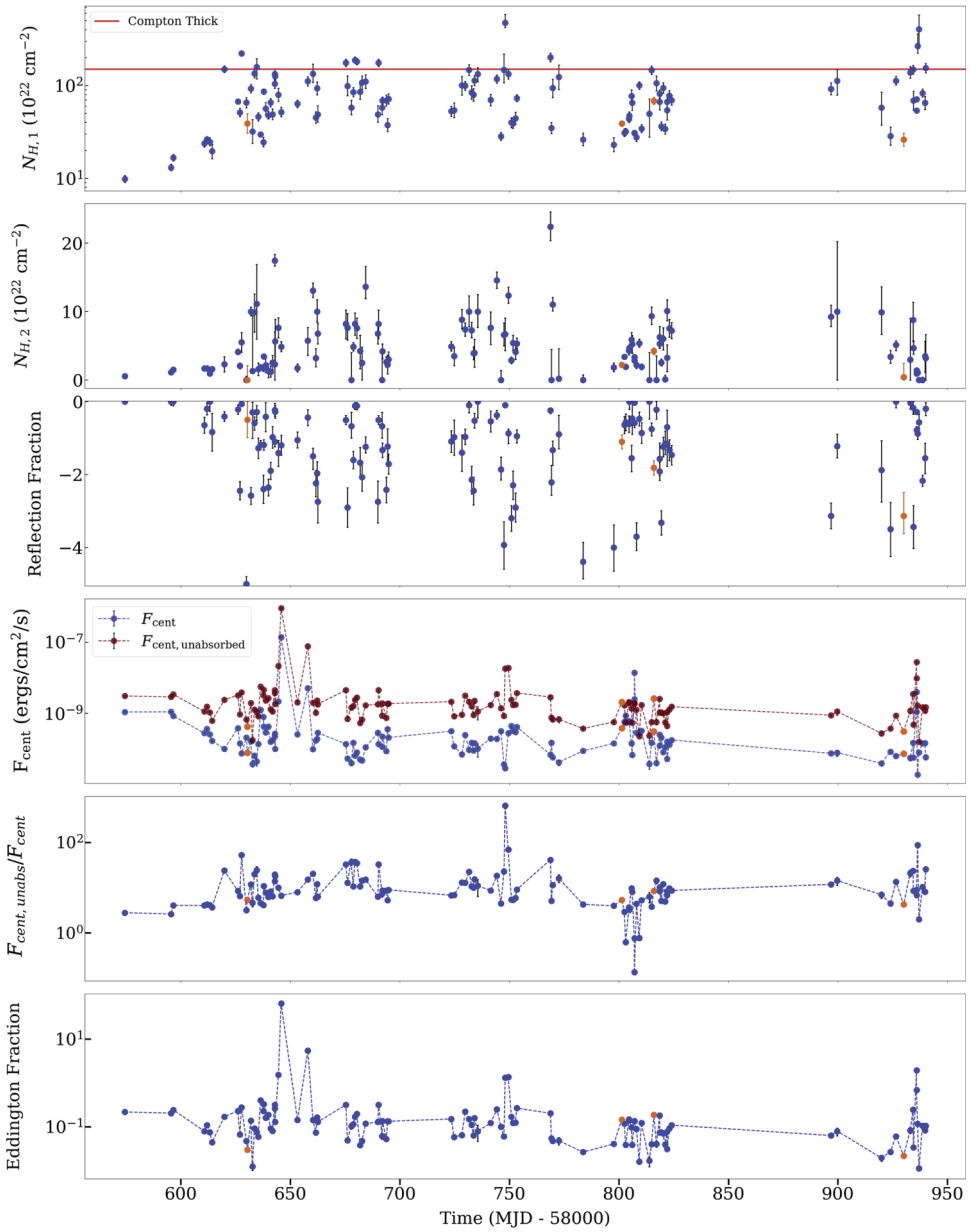

FIGURE 1.26: Results of X-ray spectral analysis of GRS 1915+105. From Balakrishnan et al. (2021).

Chapter 2

Observation and Data Reduction

Our study is based on original data in near infrared (NIR) and radio bands, in addition to the public X-ray data. The NIR data were obtained and analyzed on myself, and the radio data were provided by collaborators. For this reason, NIR observations and NIR data analysis are described in detail in the following sections. Figure 2.1 shows the NIR and radio observation periods. The NIR and radio periods are from 2019-04-02 to 2020-11-12 and from 2019-02-15 to 2019-12-03, respectively.

2.1 Kanata telescope

Kanata telescope of the Higashi-Hiroshima Observatory is the fifth largest optical-infrared telescope in Japan with a primary mirror of 1.5 m. Figure 2.2 shows the Kanata telescope. One of the most unique features of the Kanata telescope is its operating speed (see Table 2.1). This speed is remarkably fast for a 1-m class telescope. Taking advantage of its mobility, the Kanata telescope is actively used to observe Gamma-ray bursts (GRBs), gravitational wave sources, and supernovae in particular. The Kanata telescope is also unique that it can perform polarimetry and spectroscopy observations not only in optical band but also in NIR band. With these capabilities, the telescope is also actively used for collaborative observations at multi-wavelengths in radio, X-ray and gamma-ray bands. There are currently two main instruments used in Kanata telescope observations, Howpol and HONIR. Since only HONIR was used in our study, we introduce HONIR in the following.

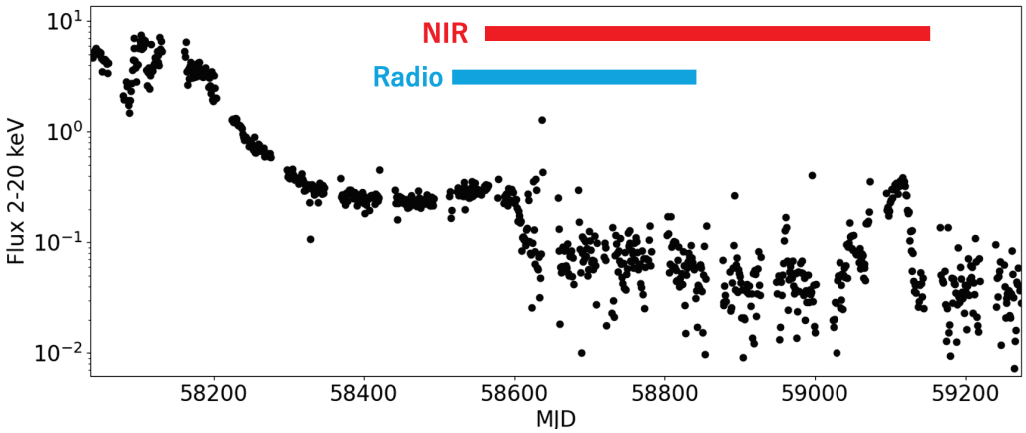

FIGURE 2.1: NIR and radio observation periods with MAXI 2 – 20 keV light curve. The horizontal bars represent the NIR (red) and radio (blue) observation periods.

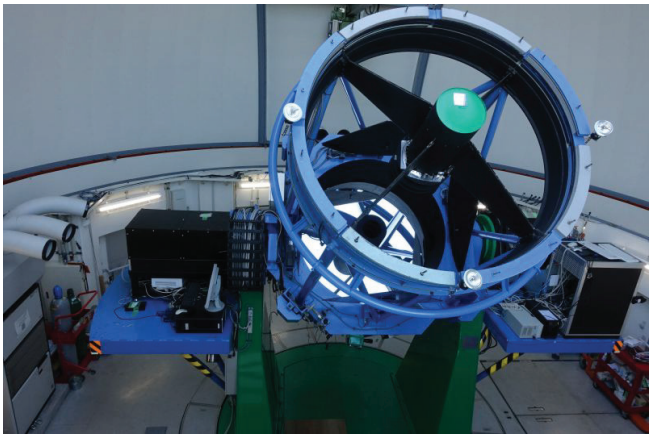

FIGURE 2.2: Picture of Kanata telescope. From https://www.hiroshima-u.ac.jp/hasc/abstract.

TABLE 2.1: Basic specifications of kanata telescope.

Item	Value
Optics	Ritchey-Chretien System
Primary Mirror	1600 mm diameter ULE glass, 983 kg
Effective Diameter	1500 mm
Composite focal length	18,501.7 mm (F/12.3)
Field of View	15 arcmin diameter
Scale at Focal Plane	11.15 arcsec/mm
Mount	Alt-Az system (friction drive)
Focus	Cassegrain, Nasmyth 1, Nasmyth 2
Operating Speed in azimuth	6 degs/sec

From http://hasc.hiroshima-u.ac.jp/telescope/kanatatel-e.html.

TABLE 2.2: Detectors of HONIR.

	Optical Arm	IR Arm
Type	CCD	HgCdTe
Pixels	2048 x 4096	2048 x 2048
Pixel Size (um)	15	20
Gain (typical) (e-/ADU)	2.7	11.6
Readout Noise (typical) (e-)	4	24
Readout Frame Rate (sec/frame)	17.4	4.5

From http://hasc.hiroshima-u.ac.jp/instruments/honir/specification/spec-e.html.

2.1.1 HONIR

Hiroshima Optical and Near-InfraRed camera (HONIR) is attached to the Kanata telescope for optical (0.5 – 1.0 μm) and NIR (1.0 – 2.0 μm) observations (Sakimoto et al., 2012; Akitaya et al., 2014). HONIR is capable of simultaneous observations in optical and NIR bands, and has three observation modes: imaging, polarimetry, and spectroscopy. HONIR has eight filters: B, V, R_C, I_C, Y, J, H, and K_S. The field of view is 10 square arc-min in the imaging mode. Other specifications of the detector are summarized in Table 2.2.

2.1.2 Data Calibration

We processed the NIR data of HONIR with Image Reduction and Analysis Facility (IRAF). IRAF is widely used to process astronomical data in optical and NIR bands. The data calibrations are described in the followings.

Dark-frame subtraction

Dark represents the noise produced by the excitation of electrons in the detector, which depends on the temperature. This noise is proportional to the exposure time. For this reason, we subtract observed images from the dark image, which is an image obtained without exposed to the sky for the same time as the observation time. This correction is dark-frame subtraction.

Flat-field correction

The sensitivity of each pixel of the detector is not uniform. This causes position-dependence of photon count detection efficiency within a single image, which makes analysis difficult. To correct this, we obtain a flat image, which is an image obtained by irradiating all pixels with the same intensity, and divide the observed image by the flat image. This flat image is taken regularly, and the flat image close to the date of the observation image is selected for the correction.

Bad-pixel correction

The HONIR detector has defective pixels (bad pixel) due to detector material problems. Since the photon count at the bad pixel is highly indeterminate, it is overwritten by using the average or median of the photon counts of the surrounding pixels.

FIGURE 2.3: Yamaguchi interferometer. From https://news.mynavi.jp/article/20160129-kddi_yamaguchi/.

2.1.3 Photometry

One of the methods to derive the flux of the object is aperture photometry. This method measures the sum of the photon counts within a certain radius around the object. This radius is determined to be 2.5 – 3 times as large as the half width at half maximum of the object. The typical radius in our study was ∼3″. The photon count of the target was converted to flux using the surrounding stars whose fluxes were catalogued in Two Micron All Sky Survey (2MASS) All-Sky Catalog (Cutri et al., 2003).

2.2 Yamaguchi interferometer

Radio data at 8.448 GHz was obtained with the Yamaguchi interferometer at Yamaguchi University. The Yamaguchi interferometer consists of two radio telescopes with a diameter of 32 m and 34 m, as shown in Figure 2.3. The typical detection limit of the Yamaguchi interferometer is 4 mJy at 6σ. The radio flux of GRS 1915+105 was derived using the nearby AGN 1920+154 of 593 mJy at 8.448 GHz.

2.3 MAXI and RXTE satellite

Soft X-ray data were obtained from the MAXI web page[1] and the RXTE web page[2], respectively.

MAXI

The Monitor of All-sky X-ray Image (MAXI) is attached to the Japanese Experiment Module on the ISS since 2009-08-15. The advantage of MAXI is that it can perform all-sky X-ray observations in ∼90 minutes, and thus can observe GRBs and X-ray novae and alert other observatories for the transient X-ray sources. In addition, since it has been in operation for more than 12 years, long-term variations in the brightness and spectrum of X-ray sources can be studied. MAXI has two types of X-ray cameras, the Gas Slit Camera (GSC) and the Solid-state Slit Camera (SSC). The

[1] http://maxi.riken.jp/star_data/J1915+109/J1915+109.html
[2] http://xte.mit.edu/asmlc/One-Day.html

TABLE 2.3: X-ray cameras of MAXI. From Matsuoka et al. (2009).

	GSC	SSC
X-ray detector	12 pieces of one-dimensional PSPC	32 chips of X-ray CCD
X-ray energy range	2 – 30 keV	0.5 – 12 keV
Total detection area	5350 cm^2	200 cm^2
Energy resolution	18% (5.9 keV)	$\leq$ 150 eV (5.9 keV)
Field of view	1.°5 x 160°	1.°5 x 90°
Detector position resolution	1 mm	0.025 mm (pixel size)
Localization accuracy	0.°1	0.°1
Absolute time resolution	0.1 ms (minimum)	5.8 s (nominal)
Weight	160 kg	11 kg

TABLE 2.4: Specifications of HEXTE. From https://heasarc.gsfc.nasa.gov/docs/xte/learning_center/hexte.html.

HEXTE Parameter	value
Energy Range	15 – 200 keV
Energy Resolution	15% at 60 keV
Time sampling	8 microsecond
Field of view	1 degree FWHM
Detectors	2 clusters of 4 Nal/Csl scintillation counters
Sensitivity	1 Crab = 360 count/s per HEXTE cluster

specifications of these two cameras are listed in Table 2.3. Since public data is only available for GSC, we used the MAXI/GSC data.

RXTE satellite

RXTE satellite is characterized by high temporal resolution (microsecond), broadband sensitivity (2 – 200 keV) and large effective area (about 0.8 m^2 total) (Bradt, Rothschild, and Swank, 1993). The mission of RXTE satellite is to study the broadband spectra and variations on timescales from microseconds to years of black holes and neutron stars and so on. RXTE satellite was launched in December 1995, and observational data until January 2012 are available. RXTE satellite has three instruments: High Energy X-ray Timing Experiment (HEXTE: 15 – 250 keV), Proportional Counter Array (PCA: 2 – 60 keV), and All Sky Monitor (ASM: 2 – 10 keV). The specifications of these instruments are listed in Tables 2.4, 2.5, and 2.6. We used 1 day averaged data of A-band (2 – 4 keV) of ASM from January 1996 to October 2011.

TABLE 2.5: Specifications of PCA. From https://heasarc.gsfc.nasa.gov/docs/xte/learning_center/pca.html.

PCA Parameter	value
Energy Range	2 – 60 keV
Energy resolution	$<$ 18% at 6 keV
Time resolution	1 microsecond
Spatial resolution	collimator with 1 degree FWHM
Detectors	5 proportional counters
Sensitivity	0.1 mCrab

TABLE 2.6: Specifications of ASM. From https://heasarc.gsfc.nasa.gov/docs/xte/learning_center/asm.html.

ASM Parameter	value
Energy Range	2 – 10 keV
Time resolution	80% of the sky every 90 minutes
Number of shadow cameras	3, each with 6×90 degrees FOV
Detectors	Xenon proportional counter, position-sensitive
Sensitivity	20 mCrab

Chapter 3

Results

3.1 Long-term

3.1.1 Historical light curve

To understand the behavior of the NIR emission of GRS 1915+105 in 2019–2020, which is the X-ray low luminous state (XLLS), the NIR fluxes were compared between 2019–2020 and before, as shown in Figure 3.1. The past NIR fluxes obtained from previously published papers were corrected for the galactic extinction with A_K=2.2 (Chapuis and Corbel, 2004). The maximum NIR flux in the past is ∼90 mJy, while the NIR flux in the 2019–2020 is above 90 mJy on some days and sometimes reach ∼300 mJy. The minimum NIR flux in the past is about ∼9 mJy (Chaty et al., 1996), while in the 2019–2020 it is ∼15 mJy.

3.1.2 Multi-wavelengths light curves

Figures 3.2 and 3.3 show the multi-wavelengths light curves for investigating the behavior of the NIR emission in XLLS. Focusing on the period when the radio and X-ray data are available,the anticorrelated variation between NIR and X-ray fluxes is found from MJD 58595 (2019 April 22) to MJD 58618 (2019 May 15). Based on these periods, we define the periods MJD<58595, 58618<MJD<58830, and 58595<MJD<58618 as XLLS1, XLLS2, and the transition period from XLLS1 to XLLS2, respectively.

In order to quantitatively investigate the timescales of the anticorrelated variation for NIR and X-ray bands, the light curves from MJD 58530 to MJD 58619 were fitted with the following exponential model.

$$F = S \times \exp((t - t_0)/\tau) + C \tag{3.1}$$

In this model, F, t, C, and τ represent a flux, time, constant, and timescale, respectively. The parameter S is fixed at -1in the X-ray band and $+1$in the NIR band to represent dimming and brightening, respectively. As a result of the fitting, the timescales τ were 15 ± 3 days for the X-ray band and 1.8 ± 0.1 days for the NIR band. To quantify the start time of the NIR and X-ray variations in the anticorrelated variation, we define the start time t_s as the time when the fitted model deviates from the mean flux by a standard deviation (blue area in Figure 3.4) of XLLS1. The t_s for X-ray and NIR bands were MJD∼58588 (2019 April 15) and MJD∼58612 (2019 May 9), respectively. From these investigations, it was found that for the anticorrelated variation, the timescale of the variation in the X-ray band was 7–10 times longer than that in the NIR band, andthe X-ray variability began ∼25 days before the NIR variability.

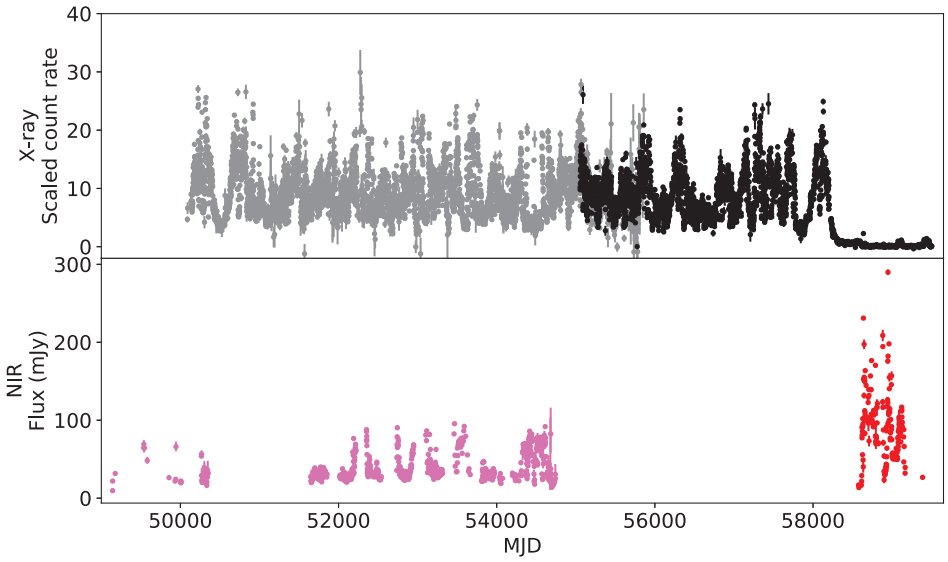

FIGURE 3.1: Historical light curves of soft X-ray and NIR bands. The upper and lower panels correspond to the X-ray and NIR light curves. The gray and black plots represent the RXTE data (1.5–2.0 keV) and the MAXI data (2.0–4.0 keV), respectively. The pink and red plots represent the previous K- and K_S-band data and our K_S-band data. NIR flux was corrected for the reddening with A_K=2.2 (Chapuis and Corbel, 2004).

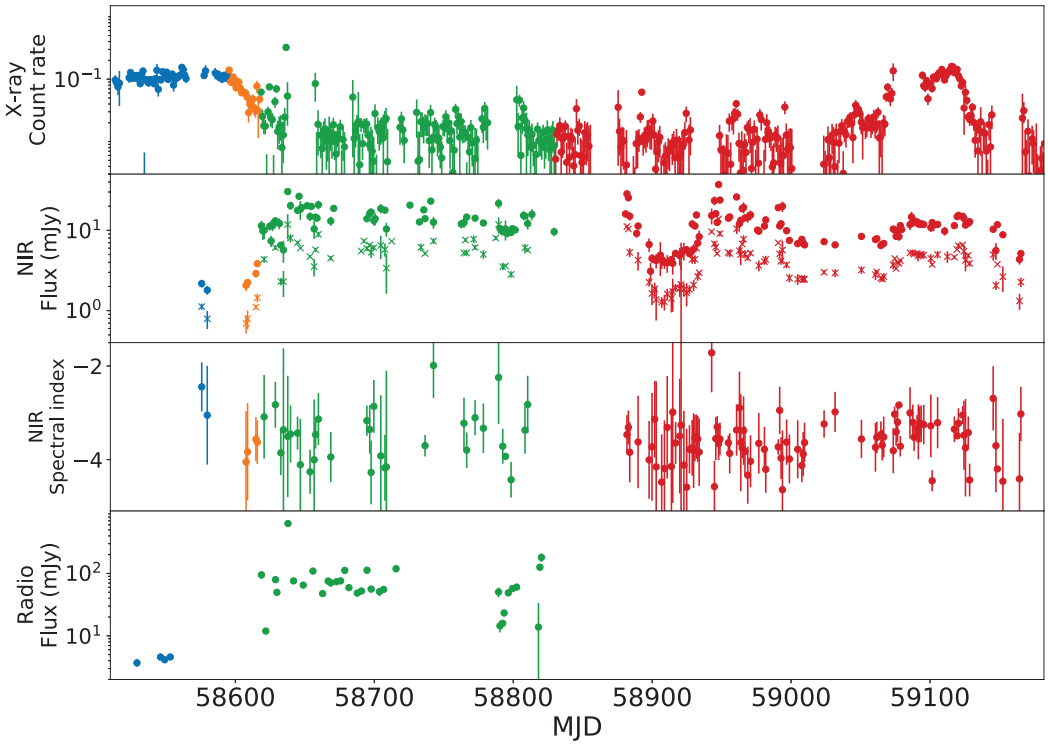

FIGURE 3.2: Multi-wavelengths light curvesin 2019–2020. From the top panel, soft X-ray count rate, NIR flux, NIR spectral index, and radio flux are shown in order. The blue, orange, green, and red plots represent XLLS1, the transition period from XLLS1 to XLLS2, XLLS2, and the period after XLLS2. In the NIR light curves, the circles and the crosses represent the K_S- and H-band fluxes, respectively.

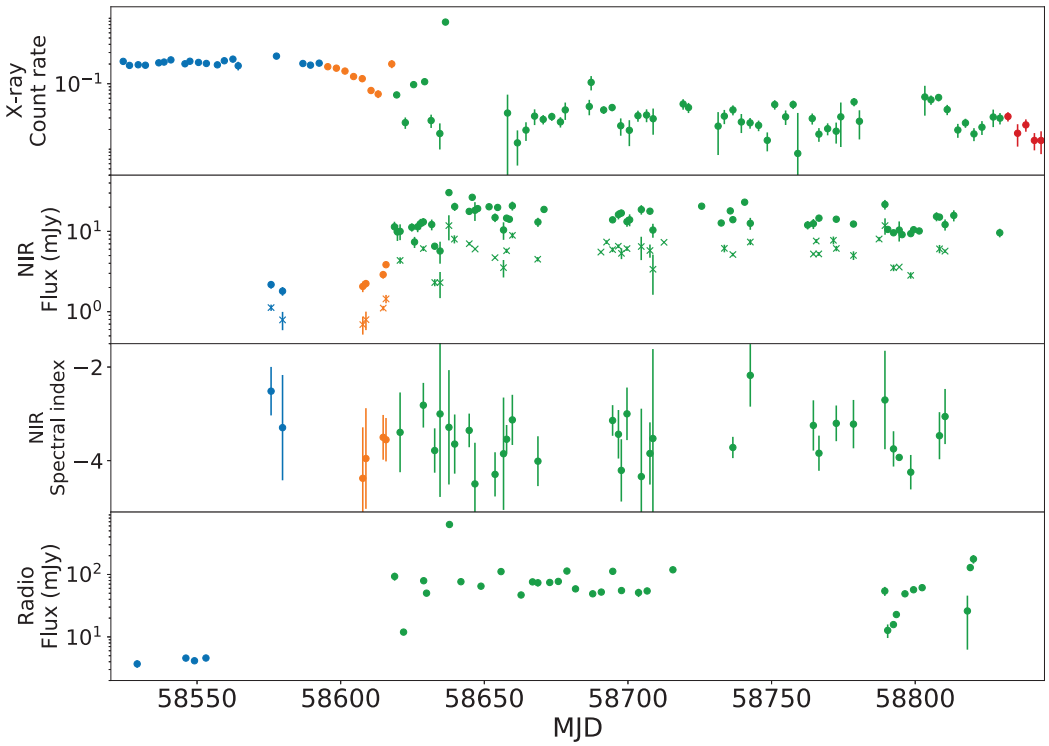

FIGURE 3.3: Enlargement light curve from XLLS1 to XLLS2 in Figure 3.2.

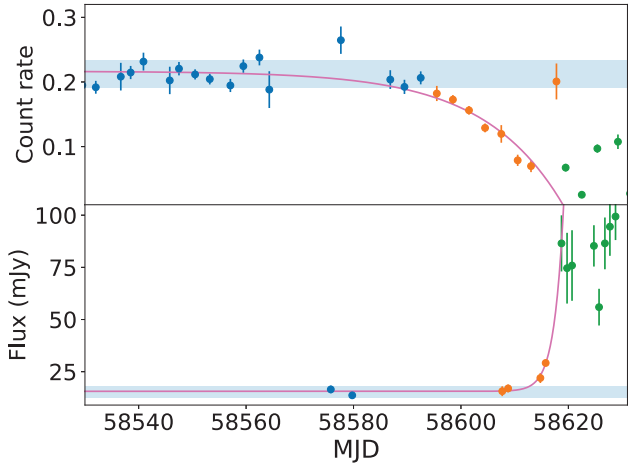

FIGURE 3.4: Fitting of the anticorrelated variations of the NIR and X-ray bands and the variation start-times and variation timescales. The blue areas in the upper and lower panels represent the mean and standard deviated area of the X-ray and NIR fluxes from MJD 58530 to MJD 58595, respectively. The pink lines represent the variation model fitted with the data from MJD 58530 to MJD 58619.

The third row of Figures 3.2 and 3.3 showthe K_S- and H-band spectral index, α_{NIR}, in XLLS. The mean and standard error and standard deviation of the NIR spectral index for XLLS1, XLLS2, the transition period from XLLS1 to XLLS2, the period after XLLS2, and the entire XLLS were -2.9 $\pm$ 0.4 and 0.6, -3.5 $\pm$ 0.1 and 0.5, -3.8 $\pm$ 0.2 and 0.4, -3.64 $\pm$ 0.05 and 0.46, and -3.61 $\pm$ 0.04 and 0.48, respectively. Therefore, the NIR spectral index of XLLS1 and XLLS2 possibly varies. However,because of the large uncertainties in each spectral index and the only two datain XLLS1, we could not conclude.

The fourth row of Figure 3.3 shows the radio flux in XLLS. The radio fluxof XLLS1 was low at $\sim$4 mJy, but it was high ($\sim$74 mJy) in XLLS2 and the high flux continued for at least $\sim$95 days in MJD 58618–58715. The result of the continuous high flux is consistent with the results of other authors(Trushkin et al., 2019; Motta et al., 2021). The radio flux level of XLLS2 is not higher than the historical flux level of $\sim$100 mJy from observations over several tens of days (Pooley and Fender, 1997; Fender et al., 1999; Rodriguez et al., 2008; Punsly and Rodriguez, 2016). Since there is no radio data during the anticorrelated variation of the NIR and X-ray fluxes, it is not clear whether the radio fluxes varied simultaneously with the NIR and X-ray fluxes.

Figure 3.5 shows the NIR and X-ray light curves after XLLS2. In the NIR band, a flare with a peak flux of $\sim$27.5 mJy was observed at MJD 58881.850–58881.873 (2020 February 2). The brightest radio flare in more than a decade also occurred at MJD 58881.319 (Trushkin et al., 2020). Note that there is no our NIR observation at the same time as the radio observation. Since there is only one NIR data before the apparent peak date of the NIR flare, it is not possible to determine the exact peak time of the NIR flare. After the NIR flare, the NIR flux became lower and was stable at $\sim$4.5mJy from MJD 58898 to MJD 58926. The radio flux was also low at that time (Motta et al., 2021). Motta et al. (2021) pointed out that the X-ray flux returned to the same level as XLLS1 and the spectrum was soft from MJD$\sim$59050 to MJD$\sim$59140. During this period, the NIR fluxes also increased, but unlike the shape of the X-ray flux variation, there was no obvious peak of the NIR fluxes. During the period, the radio flux was low (Motta et al., 2021).

3.2 Short-term

Figures 3.6 and 3.7 show examples of the short-time variability of the NIR band in 2019–2020. Some days show several flares in a few hours (e.g., 2019-06-05 in Figure 3.6 and the left panel of Figure 3.7), while other days show no variability (e.g., 2020-8-18 in Figure 3.6 and the right panel of Figure 3.7).

Figure 3.8 shows the NIR light curves within one day in 1996–2002. In all observations, flares were observed. As described in Section 1.3.3, the origin of the short-term variability is considered to be jet.

To investigate the nature of the 2019–2020 flares, we compared the flares in 2019–2020 and 1996–2002. Figure 3.9 shows a comparison of the light curves between 2019 flare and the typical past flare (Eikenberry et al., 1998). By comparing them by eye, the base fluxes appear to be stable in 1996–2002 flares (e.g., $\pm$ $\sim$1 mJy for 1997-08-14 in Figure 3.9), while they appear to be varying in 2019–2020 flares (e.g., $\pm$ $\sim$5 mJy for 2019-06-05 in Figure 3.9).

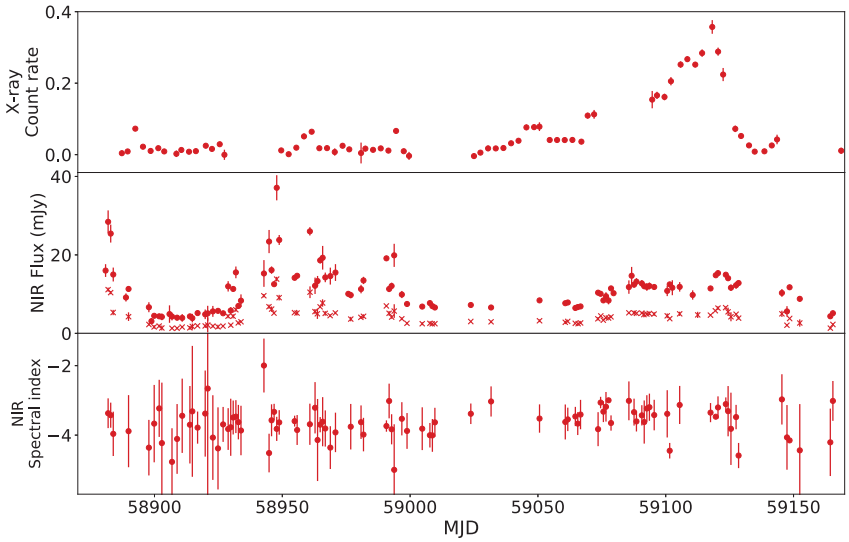

FIGURE 3.5: Light curves for the period after XLLS2 in Figure 3.1. The radio light curve is excluded since we do not have radio data for this period.

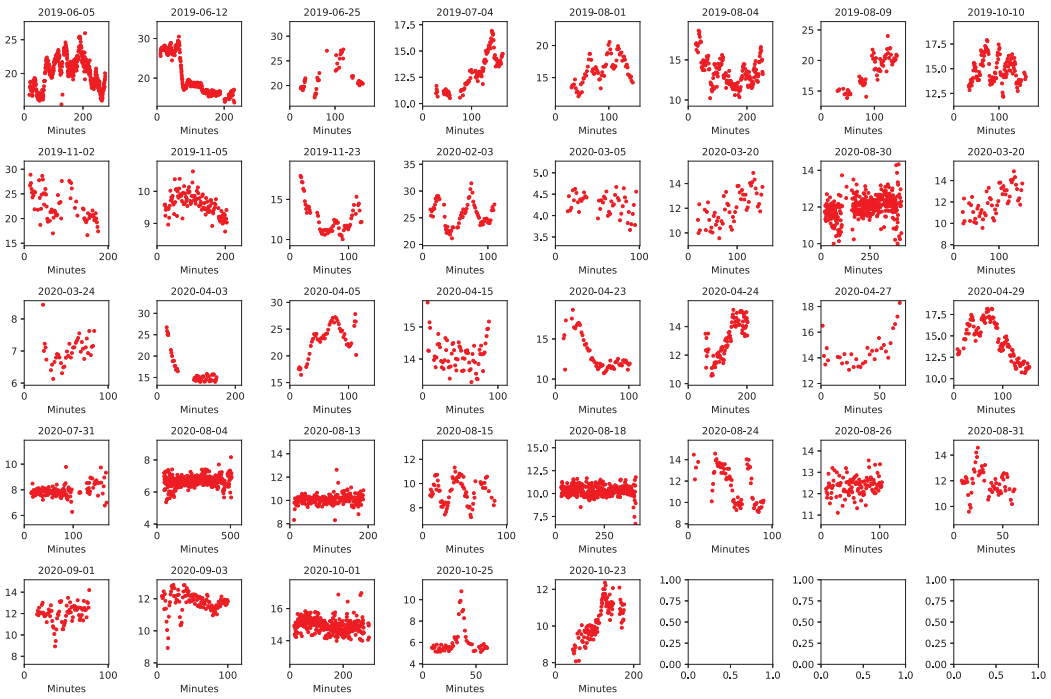

FIGURE 3.6: Examples of light curves of GRS 1915+105 within one day. The observation date is shown above each panel. The horizontal and vertical axes are time (minutes) and flux (mJy), respectively.

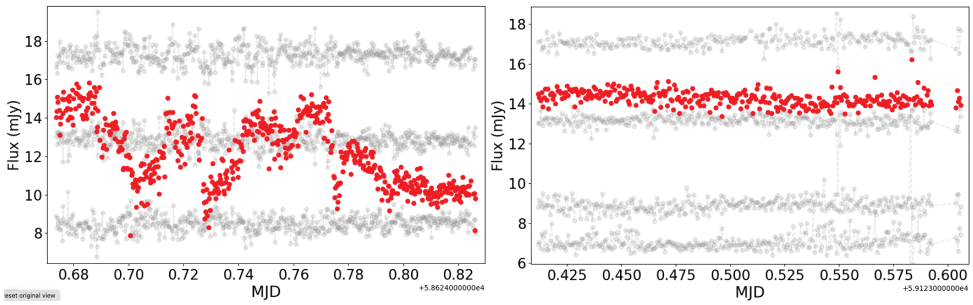

FIGURE 3.7: Examples of light curves with and without flares. The dates in the left and right panels are 2019-05-21 and 2020-10-01, respectively. The red and gray plots correspond to GRS 1915+105 and comparison stars, respectively.

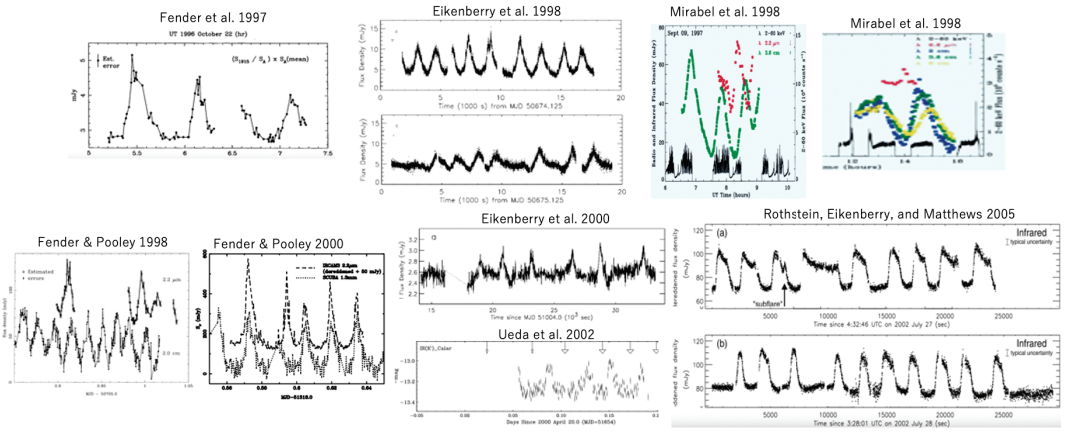

FIGURE 3.8: NIR light curves within one day from 1996 to 2002. These light curve images were obtained from Fender et al. (1997), Eikenberry et al. (1998), Mirabel et al. (1998), Fender and Pooley (1998), Fender and Pooley (2000), Eikenberry et al. (2000), Ueda et al. (2002), and Rothstein, Eikenberry, and Matthews (2005).

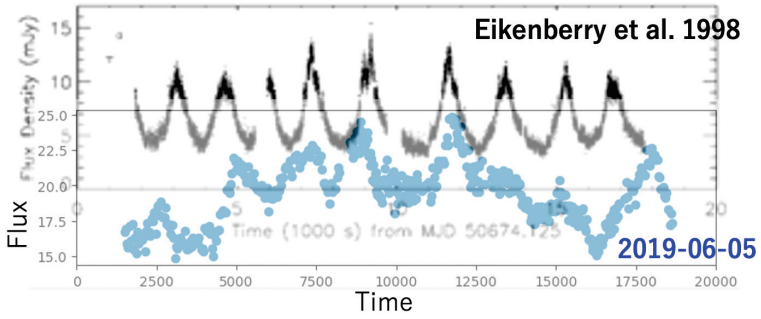

FIGURE 3.9: Overlaid light curves of the past and 2019 with obvious flares. The horizontal axes of the two light curves have the same scale and correspond to 20,000 seconds. The vertical axes have different scales. The black and blue plots are the observed data for 1997-08-14 (Eikenberry et al., 1998) and 2019-06-05, respectively.

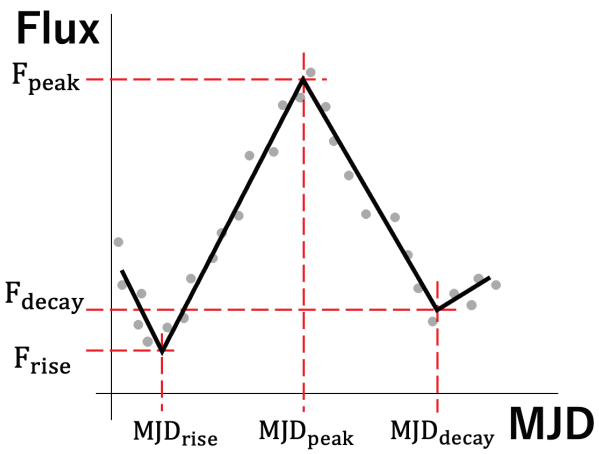

FIGURE 3.10: Explanation of the fitting function and parameters. The gray plots and black lines are the data points and the fitted model lines, respectively.

To quantitatively investigate the characteristics of the flares, the light curves are fitted with the following simple linear model for the flares in 2019 and 2020.

$$F(\mathrm{MJD}) = (F_{rise} - F_{peak})/(\mathrm{MJD}_{rise} - \mathrm{MJD}_{peak}), \quad \mathrm{MJD}_{peak} \geq \mathrm{MJD}$$
$$F(\mathrm{MJD}) = (F_{decay} - F_{peak})/(\mathrm{MJD}_{decay} - \mathrm{MJD}_{peak}), \quad \mathrm{MJD} > \mathrm{MJD}_{peak}$$

In the model, F_{peak}, F_{rise}, and F_{decay} represent the peak flux of the flare, the lowest flux of the flux rising phase, and the lowest flux of the decay phase, respectively. Also, MJD_{rise}, MJD_{peak}, and MJD_{decay} represent the start, peak, and end times of the flare, respectively. Figure 3.10 shows these parameters for a single flare. Since fitting by letting all the parameters free did not work well, MJD_{rise} and MJD_{decay} were fixed by hand and the rest of the parameters were free. Right panel of Figure 3.11 shows an example of the fitting. For 1996–2002 flares, the parameters were determined by looking at the light curve by eye, as shown in the left panel of Figure 3.11. In order to discuss the flares simply, we defined the base flux F_{base}, the amplitude F_{amp}, the rise time τ_{rise}, and the decay time τ_{rise} of the flares from the features F_{rise}, F_{peak}, F_{decay}, MJD_{rise}, MJD_{peak}, and MJD_{decay} as follows,

$$\begin{aligned} F_{base} &= (F_{rise} + F_{decay})/2 \\ F_{amp} &= F_{peak} - F_{base} \\ \tau_{rise} &= \mathrm{MJD}_{peak} - \mathrm{MJD}_{rise} \\ \tau_{decay} &= \mathrm{MJD}_{decay} - \mathrm{MJD}_{peak} \end{aligned}$$

Figure 3.12 shows the comparison of obtained flare amplitude, base flux, rise time, and decay time between 1996–2002 and 2019–2020 flares. The most obvious difference between 1996–2002 and 2019–2020 flares is the base flux. The average of base flux in 2019–2020 is $\sim$10 mJy higher than that in 1996–2002. On the other hand, there is no significant difference in flare amplitude. There was also a difference in rise time, while no significant difference in the decay time. The rise time of the 2019–2020 flares is typically longer than 20 minutes and sometimes shorter than 20 minutes, while that in 1996–2002 is all shorter than 20 minutes except one.

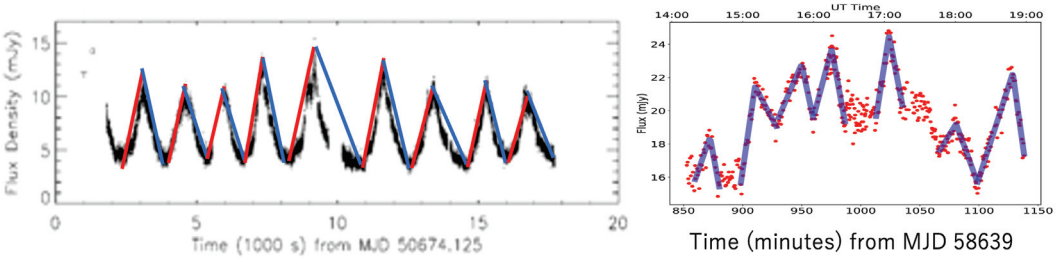

FIGURE 3.11: Examples of flare fitting. Light curve fitting for the 1997-08-14 (left) and 2019-06-05 (right) flares. The light curve in the left panel is taken from Eikenberry et al. (1998). The red and blue lines in the left panel are model lines of the phases of flux rising and decay, respectively. The blue line in the right panel is the flare model.

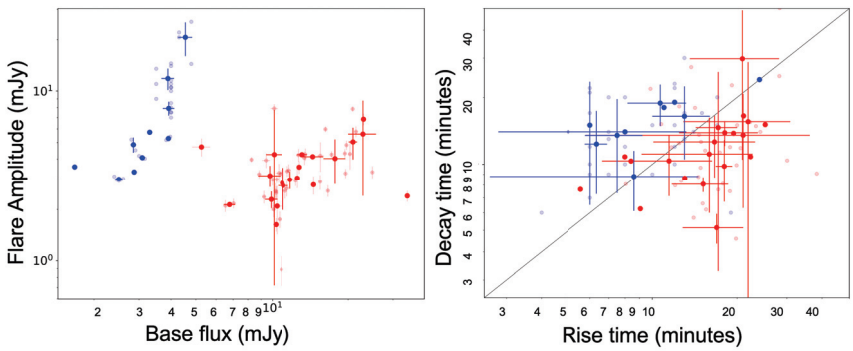

FIGURE 3.12: Comparison of obtained flare amplitude, base flux, rise time, and decay time between 1996–2002 and 2019–2020 flares. The blue and red plots correspond to 1996–2002 and 2019–2020 flares, respectively. The light and dark colors correspond to each flare and to its daily average, respectively. The solid line in the right panel is the line where rise time=decay time.

Chapter 4

Discussions

4.1 Correction for reddening of GRS 1915+105

For the interstellar absorption correction of GRS 1915+105, the extinction value at V band $A_V = 19.6 \pm 1.7$ (Chapuis and Corbel, 2004) has been widely used. This value was derived from an equation relating the total column density of the hydrogen N_H to the visual extinction, based on X-ray halo data (Predehl and Schmitt, 1995). However, a paper with another equation based on detailed study of the supernova remnant data has been published recently (Foight et al., 2016). Using the recent equation and $N_H = (3.5 \pm 0.3) \times 10^{22}$ cm^{-2} (Chapuis and Corbel, 2004), we got the visual extinction $A_V = 12.2 \pm 1.0$.

The two extinction values make it difficult to perform spectral analysis and discuss the NIR origin for the long-term and short-term variations using the spectral index. For example, the K_S- and H-band spectral index of 2 with A_V=19.6 becomes 0 with A_V=12.2. The spectral indices of 2 and 0 in the NIR band are typical values for the accretion disk and the jet, respectively.

GRS 1915+105 locates in the dusty direction from the Earth. Since both papers (Predehl and Schmitt, 1995; Foight et al., 2016) have little data in the direction of denser regions than GRS 1915+105, the visual extinction converted from the total column density of the hydrogen is estimated by extrapolation and thus has a very large uncertainty. One method to obtain the visual extinction without the N_H-A_V conversion is to identify the origin of NIR emission and then find the visual extinction that can explain the spectral change from the expected intrinsic spectral shape. However, this method is not easy because it requires simultaneous observations by three or more NIR bands.

4.2 NIR origin of the long-term component of XLLS1

The low radio flux of $\sim$4 mJy was detected by the Yamaguchi interferometer in XLLS1. In the black hole X-ray binaries, when the radio flux is low, the NIR spectrum is generally dominated by the emission from the companion star or the accretion disk. Figure 4.1 shows the radio to NIR spectra in XLLS1 with the millimeter data of Atacama Large Millimeter/submillimeter Array (ALMA) from Koljonen and Hovatta (2021). Note that the data for the centimeter, millimeter, and NIR bands are from different days of observations. The power-law component connecting the two bands was estimated by assuming that the radiation from cm to mm was a jet. Extrapolating the power-law of the jet to the NIR band, we found that it could not explain the NIR flux. As a result, the NIR origin of the long-term component of XLLS1 cannot be the jet and could be the companion star or the accretion disk.

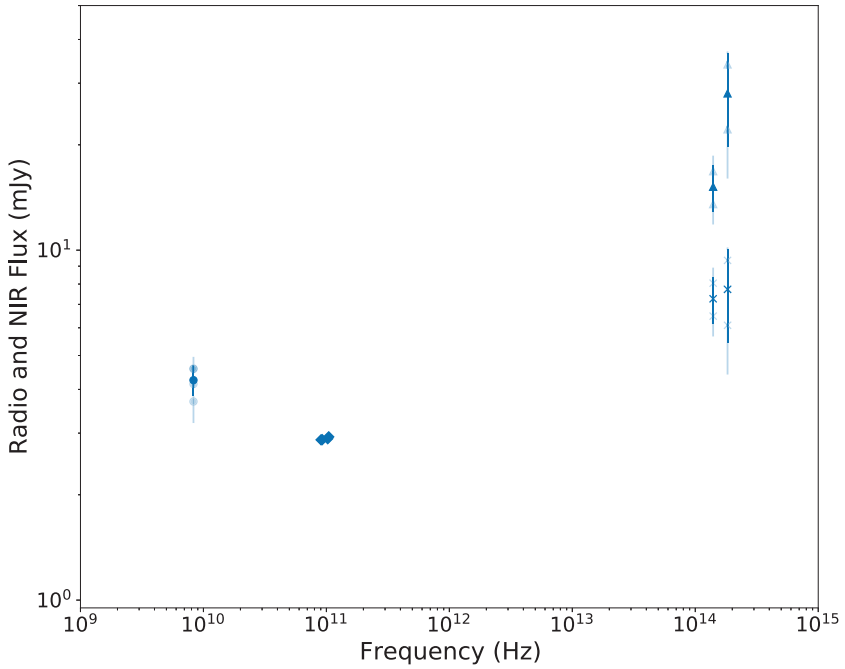

FIGURE 4.1: Centimeter, millimeter, and NIR spectra of XLLS1. The thin plots represent the daily data of XLLS1. The dark plots represent the data averaged over the period of XLLS1. There are two patterns of plots in the NIR band with the visual extinction $A_V = 12.2$ (Chapuis and Corbel, 2004) and 19.6.

4.3 NIR origin of the long-term component of XLLS2

The NIR fluxes higher than the past maximum flux level (∼90 mJy with A_V=19.6) are observed on most days, especially in 58630 < MJD < 58680, which are clearly brighter with the average flux of 150 mJy (see Figure 3.1) in XLLS2. As the NIR flux increased from XLLS1 to XLLS2, the radio flux also increased to around the maximum flux level (∼100 mJy) of the period before XLLS1. After the correlated variation, both NIR and radio fluxes were kept high for a long period of at least 95 days. These similarities with radio band suggest that the jet is one of the main origins of the NIR emission in XLLS2.

As mentioned in Section 1.3.3, the non-thermal emission, which can be interpreted as the jet, is suggested to be dominant in the NIR band at high NIR fluxes in the period before XLLS1 (Neil, Bailyn, and Cobb, 2007). Thus, the jet may be a common origin of NIR emission between XLLS2 and the period before XLLS1 of high NIR fluxes, although the maximum NIR flux levels are different. In contrast to the NIR observations, no obvious differences were found in the radio observations between the XLLS2 and the period of XLLS1. As mentioned in Section 3.1.2, the radio flux of ∼74 mJy in XLLS2 is within the maximum radio flux level of the period before XLLS1. In XLLS2, we do not have any information on the radio spectral index. But Trushkin et al. (2019) reported the spectral index of ∼-0.3 during a flare (MJD 58637.99, 2019-06-03) and we will use this to compare with that in the period before XLLS1. This spectral index in XLLS2 is consistent with the spectral index of ∼-0.4 ± 0.1 in the period before XLLS1 from the Green Bank Interferometer data at flux ranges comparable to the 2019-06-03 flare (400–500 mJy at 8 GHz). Since the radio flux and spectral index in XLLS2 are not unusual compared to those in the period

before XLLS1, it is possible that the jet emission in XLLS2 is similar to that in the period before XLLS1. If the NIR origin of the long-term component of XLLS2 is only the jet, the NIR flux should also be the same as in the period before XLLS1. Nevertheless, the NIR fluxes higher than the historical maximum flux level were found in XLLS2. This suggests that there are other NIR origins of the long-term component in addition to the jet, or that the jet emission is not similar between XLLS2 and the period before XLLS1. The suggestion that non-jet origin also contributes to the NIR band is discussed in the following paragraph. Another suggestion, that the nature of the jet is different between XLLS2 and the period before XLLS1, is discussed in Section 4.5 later.

The non-jet candidate for the NIR emission is the blackbody emission from the outer parts of the accretion disk. However, X-ray spectral analysis showed that the intrinsic X-ray flux corrected for the X-ray obscuration and the mass accretion rate did not increase from XLLS1 to XLLS2 (Balakrishnan et al., 2021). These indicate that the NIR flux of the accretion disk is not expected to increase as in XLLS2. Thus, in a simple scenario, the disk is not considered to be the NIR origin of the long-term component of XLLS2. Another possible candidate origin is the NIR emission related to the X-ray obscuration. The existence of the X-ray obscuration is confirmed by the X-ray spectral analysis (Koljonen and Tomsick, 2020; Miller et al., 2020; Neilsen et al., 2021; Balakrishnan et al., 2021), and it is augured to be caused by a puffed-up outer disk (Neilsen et al., 2021) or the disk wind at speeds below the escape velocity (Miller et al., 2020). The X-ray spectral analysis showed that the Hydrogen column density of the X-ray obscuration increased by about one order of magnitude (Balakrishnan et al., 2021) from the period before XLLS1 to XLLS2 (see Figure 1.26 and Section 1.3.4), and becomes Compton-thick (this corresponds to the red line in the top panel of Figure 1.26) around the beginning of XLLS2. The increase period of the density roughly coincides with the NIR brightening period.

There are two scenarios of NIR brightening due to the X-ray obscuration that have already been proposed to explain the anticorrelated variation between X-ray and optical/NIR fluxes in the 2005 outburst (Markwardt and Swank, 2005) of the black hole X-ray binary, GRO J1655-40 (Zhang et al., 1994; Wilson et al., 1994; Bailyn et al., 1994). The first scenario is that the X-ray obscuration emits NIR radiation (Neilsen et al., 2016). In this scenario, the temperature of the X-ray obscuration increases due to the X-ray photons of the inner parts of the disk, and the blackbody radiation of the X-ray obscuration contributes to the NIR band. The second scenario is that the X-ray obscuration increases the efficiency of the reprocessing (Shidatsu, Done, and Ueda, 2016). In this scenario, the X-ray photons of the inner disk are scattered with the X-ray obscuration. This causes more X-ray photons to irradiate the outer disk than usual, which increase the temperature of the outer disk. The higher temperature disk contributes to the NIR band by more blackbody radiation than usual. Since either or both of these mechanisms are thought to occur in GRO J1655-40 in the super-Eddington state (Neilsen et al., 2016; Shidatsu, Done, and Ueda, 2016), if either of these mechanisms also occur in GRS 1915+105, then GRS 1915+105 may also be in the super-Eddington state.

4.4 Similarities of NIR emission between XLLS2 and the 2007 soft state

The anticorrelated flux variation between X-ray and NIR bands, which occurred in the middle of 2019, is not the first case. Arai et al. (2009) reported an anticorrelated

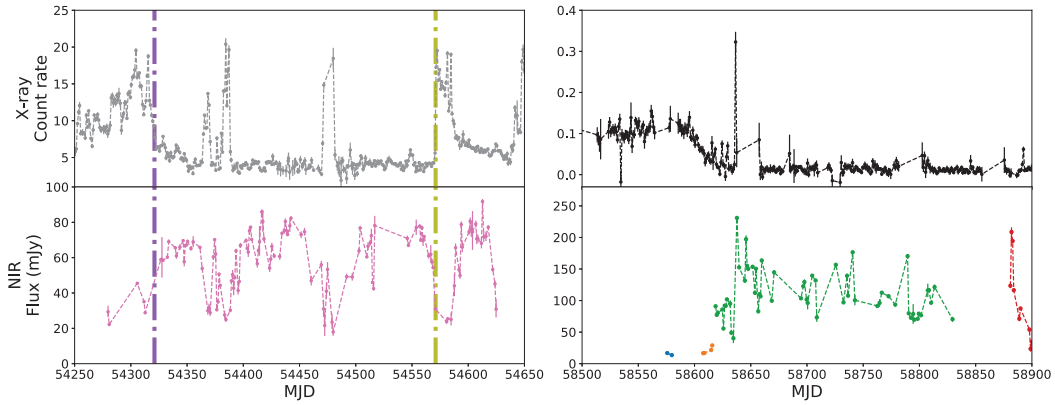

FIGURE 4.2: Soft X-ray and K_S light curves. Left and right panels correspond to the 2007 soft state and XLLS.
Data are the same as in Figures 3.1 and 3.3. In the left panel, the period between the purple and yellow dashed-dotted lines is the soft state. The K_S flux was corrected for the reddening with A_K=2.2 (Chapuis and Corbel, 2004).

flux variation pattern between X-ray and NIR bands during the soft state in 2007; the NIR magnitude decreased more than one order of magnitude during X-ray flares of several days, as shown in Figure 4.2.

There was another anticorrelated variation during the transition to the 2007 soft state (the period around the purple line in Figure 4.2) that they did not mention. After the anticorrelated flux variation, the X-ray and NIR fluxes remain low and high, respectively, for a long period of time (∼250 days, Arai et al. (2009)). This is similar to the characteristic of the period after the anticorrelated variation of XLLS (at least over 200 days). Another similarity is that the NIR spectral indices after the anticorrelated variations in the soft state in 2007 and XLLS2 are roughly consistent. The spectral indices between K_S- and H-fluxes in the 2007 soft state and XLLS2 are -3.5 $\pm$ 0.3 and -3.5 $\pm$ 0.1, respectively. Not only NIR band, but also X-ray band has a similarity; in the 2007 soft state and XLLS2, the spectral analysis suggests the presence of the X-ray obscuration (Ueda, Yamaoka, and Remillard, 2009; Neilsen et al., 2016; Balakrishnan et al., 2021).

Although the three similarities exist in the periods after the anticorrelated variations of the 2007 soft state and XLLS2, three clear differences also exist. The first difference is the X-ray hardness ratio between the two periods: the spectrum was soft in the 2007 soft state while it was hard in XLLS2 (Koljonen and Tomsick, 2020; Motta et al., 2021). This can be interpreted as the difference in the intrinsic X-ray spectrum of the inner parts of the disk. The second is the difference of multi-wavelength variation pattern between two periods. While the NIR flux decreased when the X-ray and radio flux increased in the 2007 soft state (MJD $\sim$ 54365) (Arai et al., 2009), the flux increased in all the wavelength bands in XLLS2 (MJD $\sim$ 58637). The reason for the difference is unclear. The third is the difference in the radio flux, which was lower in the 2007 soft state (Arai et al., 2009) while it was higher in XLLS2. This difference may come from the presence or absence of the jet due to the difference in the mass accretion rate. The X-ray spectrum analysis gives mass accretion rates of 30% – 120% for the 2007 soft state (Ueda, Yamaoka, and Remillard, 2009) and 1% – ∼10% for XLLS2 (Koljonen and Tomsick, 2020; Balakrishnan et al., 2021). In XLLS2, the mass accretion rate is lower than that of the 2007 soft state. In general, the stable jet is (not) observed in the hard state (soft state) in the X-ray binaries.

Because of the three similarities despite some clear differences, the 2007 soft state and XLLS2 possibly have a common NIR origin. As mentioned in Section 4.3, the NIR emission in XLLS2 may come from the jet and be caused by the X-ray obscuration. Since the radio flux in the 2007 soft state was low in contrast to that in XLLS2, the jet is not the main origin of the NIR emission in the 2007 soft state. Therefore, there is a possibility of the emission caused by the X-ray obscuration could have contributed to the NIR band in the 2007 soft state.

If the Eddington fraction in XLLS2 is really $\sim$10% (Balakrishnan et al., 2021), it corresponds to a typical value of the soft state. This has already been pointed out by Balakrishnan et al. (2021). We found further evidences for the soft state, such as the X-ray and NIR anticorrelated variation and subsequent flux characteristics that were also seen during and after the transition to the 2007 soft state. However, the bright and stable jet that may contribute to the NIR band is the characteristic of the hard state (see Section 1.2). Then, the combination of the soft state characteristics and the hard state characteristics suggests that GRS 1915+105 in XLLS2 may be a new state that is neither the soft state nor the hard state.

4.5 Base line flux of short-term variation between the period before XLLS1 and 2019–2020

In all of the flares of the period before XLLS1, there is a clear single base line with a constant flux that can be seen throughout several hours of the NIR observations (Fender et al., 1997; Eikenberry et al., 1998; Fender and Pooley, 2000; Eikenberry et al., 2000; Ueda et al., 2002; Rothstein, Eikenberry, and Matthews, 2005). However, in the 2019–2020 flares, there is no clear base line on some days. Even though there is a base line on some days, the base line flux is not constant and varies. Compared to the flares in the period before XLLS1, the base line flux of the 2019–2020 flares is clearly higher. On the other hand, there is no clear difference in the amplitude and decay time of the flares between the two periods. The rise time of the flare may be different between the two periods, but this difference is possibly due to the difference of the measurement method.

In the period before XLLS1, the NIR origin of the short-term component is considered to be the jet (see Section 1.3.3). The lack of clear differences in the features other than the base line flux between two periods suggests the jet as one of the origins of the short-time variation of the 2019–2020 flares. Taking the discussion into account, there are two scenarios that can explain the higher and less stable base line flux in 2019–2020 compared to that in the period before XLLS1.

1. The jet is only the origin of the short-term variation in the period before XLLS1 and 2019–2020, but the nature of the jet is different between the two periods (jet-only scenario).

2. The jet is only the origin of the short-term variation in the period before XLLS1, while the jet and another origin with a longer timescale than the jet is the origin of the short-term variation in 2019–2020 (jet-and-another-origin scenario).

In the jet-only scenario, a possible cause of the changes in the base line flux in 2019–2020 is that the next flare starts before the decays of the previous flare. In this situation, the observed flux does not drop to the base line flux of the period before XLLS1, but remains high because the flux of the next flare is added before the decaying of the previous flare before the flux (not the observed flux) of the decaying flare

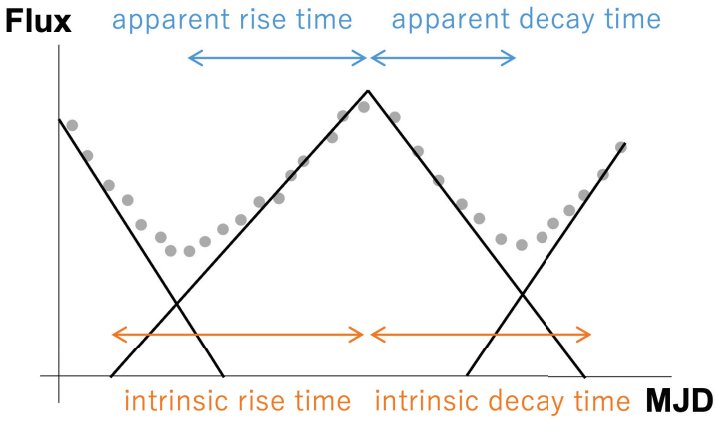

FIGURE 4.3: Explanation of the apparent and intrinsic times. The gray plots and black lines are the observed fluxes and the flares, respectively. The blue and orange arrows represent the apparent and intrinsic times of the flare, respectively.

reaches zero. The reason for the overlap of flares could be that the time interval of flare occurrence is shorter in 2019–2020, or the intrinsic rise and decay times of the flares are longer in 2019–2020. The intrinsic rise and decay times mean the rise and decay times that can be measured when the flares do not overlap. To avoid confusion, the jet-only scenario refers to the rise and decay times measured in Section 3.2 as the apparent rise and decay times. Explanation of these times is shown in Figure 4.3. A comparison of time intervals of flares between 2019–2020 and the period before XLLS1 is shown in Figure 4.4. The time intervals of flares were calculated from the peak times of neighboring flares. The result shows that the time interval for the 2019–2020 flares was not shorter than that of the period before XLLS1. This means that the difference of the base line flux between the two periods is not due to the change of the time interval of flares.

It is possible that there is a difference of the intrinsic timescale between the two periods. The difference of the intrinsic timescale is expected to make a difference not only of the base line flux, but also of the apparent shape of the flare. Some of the flares in the period before XLLS1 (Eikenberry et al., 1998; Fender and Pooley, 2000) have an exponential shape (see Figures 3.6 and 3.9). If the intrinsic timescale of the 2019–2020 flares is longer than that of the period before XLLS1 and the flares overlap, the apparent shape of the flares becomes closer to a straight line because the shape of the exponential tail is buried. In fact, the shape of the observed 2019–2020 flare resembles a straight line (see Figure 3.9). The upper panel of Figure 4.5 reproduces the flare of Eikenberry et al. (1998) of the period before XLLS1 with the flare model (Shah et al., 2021) with rough hand-set parameters. The rise and decay timescales of the flare model are the same for each flare. The lower panel of Figure 4.5 shows the model with same parameter values except the rise and decay timescales in the upper panel. The rise and decay timescales are multiplied by 2.5 to the rise and decay timescales of the flare model of the period before XLLS1. The reproduced flares in the lower panel have the characteristics of the 2019–2020 flare: high and variable base line flux. The successful reproduction of these characteristics, though rough, suggests that there may be a difference in the intrinsic rise and decay timescales between XLLS2 and the period before XLLS1. This could be verified by comparing the intrinsic timescale of radio flares between the period before XLLS1 and 2019–2020 to test the scenario.

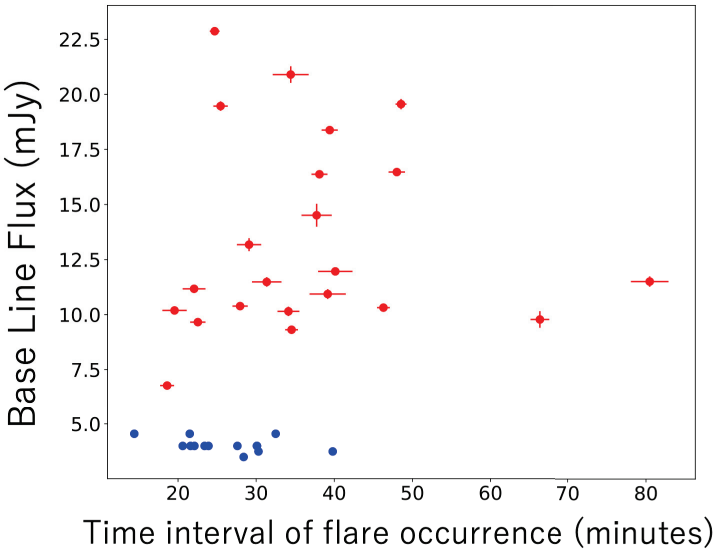

FIGURE 4.4: Comparison of Time interval of flare occurrence and base line flux between the period before XLLS1 (blue) and XLL2 (red) flares.

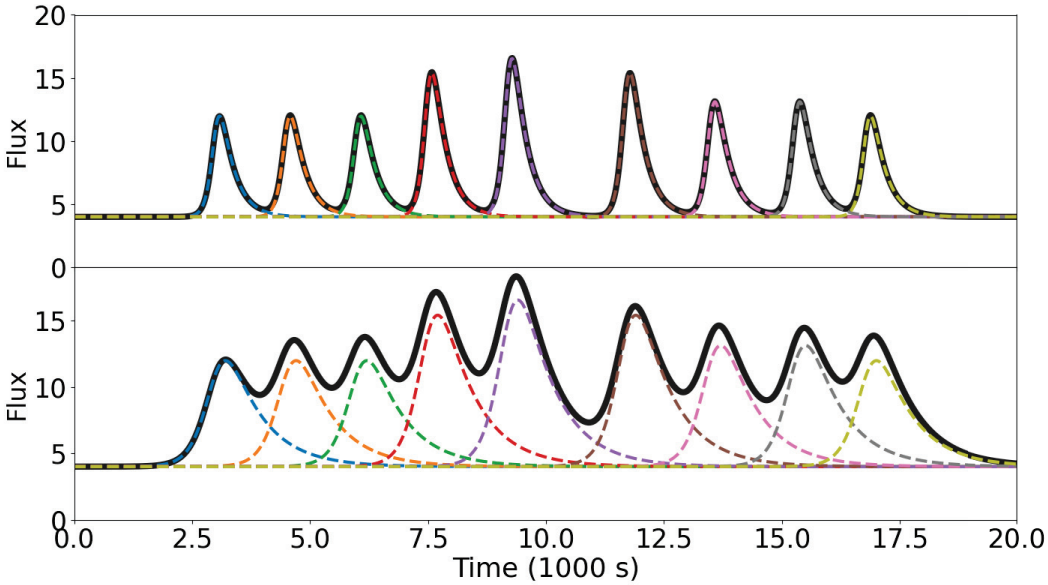

FIGURE 4.5: Reproduction of the flares of 1997-08-14 (Eikenberry et al., 1998) (upper panel) and 2019-06-05 (lower panel). Dotted and solid black lines represent each flare and their summation, respectively. The model for the flares is referred to (Shah et al., 2021), and the base flux was fixed to 4 mJy.

In the jet-and-another-origin scenario, another origin could be the X-ray obscuration as described in Section 4.3. In this situation, in XLLS2, the NIR flux of the jet is expected to be less than ∼90 mJy of the maximum flux in the period before XLLS1, since the jet has the same nature between two periods. The average NIR flux in the particularly bright period of XLLS2 was ∼150 mJy, which implies that the NIR flux of the X-ray obscuration in XLLS2 is in the range of 0–60 mJy. As mentioned in Section 4.4, in the 2007 soft state, the main NIR origin could be the X-ray obscuration, and the maximum flux level was ∼80 mJy (with A_V=19.6). The expected flux range of the X-ray obscuration in XLLS2 is 0–60 mJy, which is possibly within the maximum flux level of the 2007 soft state. Thus, we could not find any strange points in the scenario.

In summary, the high and variable base line fluxes of the 2019–2020 flares suggest two possible scenarios, neither of which can be ruled out. However, at least there is no obvious difference in the time interval of flares, indicating that the jet eruption did not occur more frequently in 2019–2020 than in the period before XLLS1 and was not caused by the difference of the base line flux. Note that we do not rule out that the difference of the intrinsic rise and decay timescales is the cause of the difference of the base line flux, and thus we also do not rule out the jet-only-scenario.

Chapter 5

Conclusions

In order to understand the NIR behavior and the origin of the NIR emission of black hole low mass X-ray binary GRS 1915+105 in the X-ray low luminous state (XLLS) observed in MAXI and RXTE (Negoro et al., 2018; Homan et al., 2019), we performed the NIR-band monitoring observation with the Kanata telescope at the Higashi-Hiroshima Observatory from April 2019 to November 2020.

We defined XLLS1 and XLLS2 as the periods before and after the X-ray dimming that occurred from MJD 58595 (2019 April 22) to MJD 58618 (2019 May 15), respectively. Focusing on the long-term variations, the followings were found. Comparing with the NIR flux until 2008, the NIR flux in XLLS2 was higher than the past maximum flux level of $\sim$90 mJy. A more detailed investigation of the NIR variation in XLLS showed that there was the NIR brightening and the X-ray dimming during the transition from XLLS1 to XLLS2. During the anticorrelated variation, the decrease of the X-ray flux started $\sim$25 days earlier than the increase of the NIR flux, and the variation timescale of the X-ray flux was 7–10 times longer than that of the NIR flux. The radio flux showed a similar flux increase to the NIR flux; the radio flux was $\sim$4 mJy in XLLS1, and $\sim$74 mJy in XLLS2. Focusing on the short-term variations, in XLLS2, some days showed clear flares, while on other days flare was absent. The base line flux of the flare was clearly higher and more variable than that of the 1996–2002 flares. On the other hand, there was no obvious difference of the rise and decay timescales and amplitude of the flare.

In XLLS1, the spectrum based on the radio to NIR data suggests that the origin of the NIR emission is not the jet but the disk or the companion star. In XLLS2, the similarity of the long-term variation between the radio and NIR bands suggests that one of the origins of the NIR emission is the jet. This is also suggested by the similarities of the characteristics of the short-term variation between XLLS2 and the 1996–2002 except for the base line flux; the latter is thought to be of the jet origin.

Based on the characteristics of the NIR and X-ray bands, which were also seen in the 2007 soft state of GRS 1915+105 (Arai et al., 2009), and the Eddington fraction $\sim$10% obtained from the X-ray spectral analysis (Balakrishnan et al., 2021), the XLLS2 of GRS 1915+105 can be interpreted as the soft state. However, the characteristic of the hard state such as the high flux of the steady jet, which possibly contributes to the NIR band, suggests that GRS 1915+105 during XLLS2 may be a new state with both soft and hard state characteristics. This is contrary to the general picture of the relationship between the jet eruption and the state of the accretion disk in X-ray binaries, and thus our study provided a new observational insight into the jet eruption process under the conditions of the accretion disk.

Acknowledgements

Thanks to many people, I was able to graduate. First of all, I want to express my greatest gratitude to Prof. Fukasawa. He taught me astronomy for six years. He also revised my poor English and helped me a lot in applying for grants. I am very grateful to him for taking his precious time out of his busy schedule to help me. Next, I would like to express my gratitude to Sasada-san. I was very lucky to have met him. He taught me a lot about astronomy, observation, and how to write papers. Without his support, I could never have graduated. Next, I would like to thank Hirotaka-san. He was very tough, kind and looked like a superman. If I had any questions, I could easily ask him. It was very reassuring to have his advice before my doctoral thesis presentation. I would like to thank Nakaoka-san for his help with the observations and data analysis of the Kanata telescope. He has been working (observing) at night for many years, which I could not do, and I honestly thought he was an amazing person. I was able to get good quality data of GRS 1915+105 because of his help. I am very grateful to Uemura-san for teaching me AGN and statistics. He also taught me a lot of knowledge about the accretion disk and the companion star, which was very helpful in my research. I would also like to thank Akitaya-san for his help. He taught me a lot about polarization and observations. I enjoyed Akitaya-san's old stories about big-name researchers. I am waiting for your YouTuber debut. I would like to thank Prof. Kawabata for his help in OISTER-related issues and for allowing me to observe GRS 1915+105 for long term and sudden events. I also want to thank Prof. Fujisawa and Akimoto-san of Yamaguchi University. It was my first time to collaborate with students from other universities and I caused them a lot of trouble, but they gladly provided me with radio data. I was particularly nervous about simultaneous multi-wavelength observations of radio and NIR bands, but it was a very good experience to work together. Akimoto-san and I frequently shared data and discussed the results on slack and he was very helpful. Without their help, I would not have been satisfied with my research. Akimoto-san, please take care of yourself and do your best in your doctoral program. I am also very grateful to the current and already graduated members of our group. Please continue to take care of your health and do your best in your research, B4, M1, M2, D1, Yang Chong. I would like to thank the physics office staff for all their help and support. Especially this year, I have been working full-time remotely, which has caused you a lot of trouble. I am sorry for that. Finally, I would like to thank my family for their support.

Bibliography

Abramowicz, M. A. et al. (Sept. 1988). "Slim Accretion Disks". In: ApJ 332, p. 646. DOI: 10.1086/166683.

Akitaya, Hiroshi et al. (Aug. 2014). "HONIR: an optical and near-infrared simultaneous imager, spectrograph, and polarimeter for the 1.5-m Kanata telescope". In: *Ground-based and Airborne Instrumentation for Astronomy V*. Ed. by Suzanne K. Ramsay, Ian S. McLean, and Hideki Takami. Vol. 9147. Society of Photo-Optical Instrumentation Engineers (SPIE) Conference Series, 91474O, 91474O. DOI: 10.1117/12.2054577.

Arai, Akira et al. (June 2009). "Anti-Correlation of Near-Infrared and X-Ray Variations of the Microquasar GRS 1915+105 in the Soft State". In: PASJ 61, p. L1. DOI: 10.1093/pasj/61.3.L1. arXiv: 0904.1020 [astro-ph.HE].

Bailyn, C. et al. (Aug. 1994). "X-Ray Nova in Scorpius". In: IAU Circ. 6060, p. 1.

Balakrishnan, M. et al. (Mar. 2021). "The Novel Obscured State of the Stellar-mass Black Hole GRS 1915+105". In: ApJ 909.1, 41, p. 41. DOI: 10.3847/1538-4357/abd6cb. arXiv: 2012.15033 [astro-ph.HE].

Begelman, M. C., C. F. McKee, and G. A. Shields (Aug. 1983). "Compton heated winds and coronae above accretion disks. I. Dynamics." In: ApJ 271, pp. 70–88. DOI: 10.1086/161178.

Belloni, T. et al. (Apr. 1997). "An Unstable Central Disk in the Superluminal Black Hole X-Ray Binary GRS 1915+105". In: ApJ 479.2, pp. L145–L148. DOI: 10.1086/310595. arXiv: astro-ph/9702048 [astro-ph].

Belloni, T. et al. (Mar. 2000). "A model-independent analysis of the variability of GRS 1915+105". In: A&A 355, pp. 271–290. arXiv: astro-ph/0001103 [astro-ph].

Blandford, R. D. and A. Königl (Aug. 1979). "Relativistic jets as compact radio sources." In: ApJ 232, pp. 34–48. DOI: 10.1086/157262.

Bradt, H. V., R. E. Rothschild, and J. H. Swank (Jan. 1993). "X-ray timing explorer mission". In: A&AS 97.1, pp. 355–360.

Castro-Tirado, A. J., S. Brandt, and N. Lund (Aug. 1992). "GRS 1915+105". In: *IAU Cirulars* 5590, p. 2.

Chapuis, C. and S. Corbel (Feb. 2004). "On the optical extinction and distance of <ASTROBJ>GRS 1915+105</ASTROBJ>". In: A&A 414, pp. 659–665. DOI: 10.1051/0004-6361:20034028. arXiv: astro-ph/0310680 [astro-ph].

Chaty, S. et al. (June 1996). "Infrared and millimeter observations of the galactic superluminal source GRS 1915+105." In: A&A 310, pp. 825–830. arXiv: astro-ph/9612244 [astro-ph].

Cordova, F. A. and K. O. Mason (Sept. 1982). "High-velocity winds from a dwarf nova during outburst." In: ApJ 260, pp. 716–721. DOI: 10.1086/160291.

Cutri, R. M. et al. (2003). *2MASS All Sky Catalog of point sources.*

Dhawan, V., I. F. Mirabel, and L. F. Rodríguez (Nov. 2000). "AU-Scale Synchrotron Jets and Superluminal Ejecta in GRS 1915+105". In: ApJ 543.1, pp. 373–385. DOI: 10.1086/317088. arXiv: astro-ph/0006086 [astro-ph].

Drappeau, S. et al. (Apr. 2017). "Dark jets in the soft X-ray state of black hole binaries?" In: MNRAS 466.4, pp. 4272–4278. DOI: 10.1093/mnras/stw3277. arXiv: 1612.06896 [astro-ph.HE].

Eikenberry, S. S. et al. (Mar. 2000). "Faint Infrared Flares from the Microquasar GRS 1915+105". In: ApJ 532.1, pp. L33–L36. DOI: 10.1086/312559. arXiv: astro-ph/0001472 [astro-ph].

Eikenberry, Stephen S. et al. (Feb. 1998). "Evidence for a Disk-Jet Interaction in the Microquasar GRS 1915+105". In: ApJ 494.1, pp. L61–L64. DOI: 10.1086/311158. arXiv: astro-ph/9710374 [astro-ph].

Eikenberry, Stephen S. et al. (May 2008). "HST NICMOS Observations of Fast Infrared Flickering in the Microquasar GRS 1915+105". In: ApJ 678.1, pp. 369–375. DOI: 10.1086/523682. arXiv: 0709.1095 [astro-ph].

Esin, Ann A., Jeffrey E. McClintock, and Ramesh Narayan (Nov. 1997). "Advection-Dominated Accretion and the Spectral States of Black Hole X-Ray Binaries: Application to Nova Muscae 1991". In: ApJ 489.2, pp. 865–889. DOI: 10.1086/304829. arXiv: astro-ph/9705237 [astro-ph].

Fender, R. P., T. M. Belloni, and E. Gallo (Dec. 2004). "Towards a unified model for black hole X-ray binary jets". In: MNRAS 355.4, pp. 1105–1118. DOI: 10.1111/j.1365-2966.2004.08384.x. arXiv: astro-ph/0409360 [astro-ph].

Fender, R. P. and G. G. Pooley (Oct. 1998). "Infrared synchrotron oscillations in GRS 1915+105". In: MNRAS 300.2, pp. 573–576. DOI: 10.1046/j.1365-8711.1998.01921.x. arXiv: astro-ph/9806073 [astro-ph].

— (Oct. 2000). "Giant repeated ejections from GRS 1915+105". In: MNRAS 318.1, pp. L1–L5. DOI: 10.1046/j.1365-8711.2000.03847.x. arXiv: astro-ph/0006278 [astro-ph].

Fender, R. P. et al. (Oct. 1997). "Rapid infrared flares in GRS 1915+105: evidence for infrared synchrotron emission". In: MNRAS 290.4, pp. L65–L69. DOI: 10.1093/mnras/290.4.L65. arXiv: astro-ph/9707317 [astro-ph].

Fender, R. P. et al. (Apr. 1999). "MERLIN observations of relativistic ejections from GRS 1915+105". In: MNRAS 304.4, pp. 865–876. DOI: 10.1046/j.1365-8711.1999.02364.x. arXiv: astro-ph/9812150 [astro-ph].

Fender, Rob (2006). "Jets from X-ray binaries". In: *Compact stellar X-ray sources*. Vol. 39, pp. 381–419.

Fender, Rob and Tomaso Belloni (Sept. 2004). "GRS 1915+105 and the Disc-Jet Coupling in Accreting Black Hole Systems". In: ARA&A 42.1, pp. 317–364. DOI: 10.1146/annurev.astro.42.053102.134031. arXiv: astro-ph/0406483 [astro-ph].

— (Aug. 2012). "Stellar-Mass Black Holes and Ultraluminous X-ray Sources". In: *Science* 337.6094, p. 540. DOI: 10.1126/science.1221790. arXiv: 1208.1138 [astro-ph.HE].

Foight, Dillon R. et al. (July 2016). "Probing X-Ray Absorption and Optical Extinction in the Interstellar Medium Using Chandra Observations of Supernova Remnants". In: ApJ 826.1, 66, p. 66. DOI: 10.3847/0004-637X/826/1/66. arXiv: 1504.07274 [astro-ph.HE].

Foster, R. S. et al. (Aug. 1996). "Radio and X-Ray Variability of the Galactic Superluminal Source GRS 1915+105". In: ApJ 467, p. L81. DOI: 10.1086/310199.

Fuchs, Y., I. F. Mirabel, and A. Claret (June 2003). "Mid-infrared observations of GRS 1915+105 during plateau and flaring states". In: A&A 404, pp. 1011–1021. DOI: 10.1051/0004-6361:20030562. arXiv: astro-ph/0304344 [astro-ph].

Hannikainen, D. C. et al. (June 2005). "Characterizing a new class of variability in GRS 1915+105 with simultaneous INTEGRAL/RXTE observations". In: A&A

435.3, pp. 995–1004. DOI: 10.1051/0004-6361:20042250. arXiv: astro-ph/0502438 [astro-ph].

Heinz, S. and R. A. Sunyaev (Aug. 2003). "The non-linear dependence of flux on black hole mass and accretion rate in core-dominated jets". In: MNRAS 343.3, pp. L59–L64. DOI: 10.1046/j.1365-8711.2003.06918.x. arXiv: astro-ph/0305252 [astro-ph].

High Time-Resolution Astrophysics (2018). Canary Islands Winter School of Astrophysics. Cambridge University Press. DOI: 10.1017/9781316831984.

Homan, J. et al. (May 2019). "A sudden dimming of GRS 1915+105 in X-rays". In: *The Astronomer's Telegram* 12742, p. 1.

Ichimaru, S. (June 1977). "Bimodal behavior of accretion disks: theory and application to Cygnus X-1 transitions." In: ApJ 214, pp. 840–855. DOI: 10.1086/155314.

Imazato, F. et al. (May 2019). "Near-infrared observations of GRS 1915+105 in an unusual state with Kanata telescope". In: *The Astronomer's Telegram* 12765, p. 1.

Klein-Wolt, M. et al. (Apr. 2002). "Hard X-ray states and radio emission in GRS 1915+105". In: MNRAS 331.3, pp. 745–764. DOI: 10.1046/j.1365-8711.2002.05223.x. arXiv: astro-ph/0112044 [astro-ph].

Koljonen, K. I. I. and T. Hovatta (Mar. 2021). "ALMA/NICER observations of GRS 1915+105 indicate a return to a hard state". In: A&A 647, A173, A173. DOI: 10.1051/0004-6361/202039581. arXiv: 2102.00693 [astro-ph.HE].

Koljonen, K. I. I. and J. A. Tomsick (July 2020). "The obscured X-ray binaries V404 Cyg, Cyg X-3, V4641 Sgr, and GRS 1915+105". In: A&A 639, A13, A13. DOI: 10.1051/0004-6361/202037882. arXiv: 2004.08536 [astro-ph.HE].

Markoff, S., H. Falcke, and R. Fender (June 2001). "A jet model for the broadband spectrum of XTE J1118+480. Synchrotron emission from radio to X-rays in the Low/Hard spectral state". In: A&A 372, pp. L25–L28. DOI: 10.1051/0004-6361:20010420. arXiv: astro-ph/0010560 [astro-ph].

Markwardt, C. B. and J. H. Swank (Feb. 2005). "New Outburst of GRO J1655-40?" In: *The Astronomer's Telegram* 414, p. 1.

Matsuoka, Masaru et al. (Oct. 2009). "The MAXI Mission on the ISS: Science and Instruments for Monitoring All-Sky X-Ray Images". In: PASJ 61, p. 999. DOI: 10.1093/pasj/61.5.999. arXiv: 0906.0631 [astro-ph.IM].

Miller, J. M. et al. (June 2008). "The Accretion Disk Wind in the Black Hole GRO J1655-40". In: ApJ 680.2, pp. 1359–1377. DOI: 10.1086/588521. arXiv: 0802.2026 [astro-ph].

Miller, J. M. et al. (Nov. 2020). "An Obscured, Seyfert 2-like State of the Stellar-mass Black Hole GRS 1915+105 Caused by Failed Disk Winds". In: ApJ 904.1, 30, p. 30. DOI: 10.3847/1538-4357/abbb31. arXiv: 2007.07005 [astro-ph.HE].

Miller, Jon M. et al. (June 2006). "The magnetic nature of disk accretion onto black holes". In: Nature 441.7096, pp. 953–955. DOI: 10.1038/nature04912. arXiv: astro-ph/0605390 [astro-ph].

Mirabel, I. F. and L. F. Rodríguez (Sept. 1994). "A superluminal source in the Galaxy". In: Nature 371.6492, pp. 46–48. DOI: 10.1038/371046a0.

Mirabel, I. F. et al. (Feb. 1998). "Accretion instabilities and jet formation in GRS 1915+105". In: A&A 330, pp. L9–L12. arXiv: astro-ph/9711097 [astro-ph].

Mitsuda, K. et al. (Jan. 1984). "Energy spectra of low-mass binary X-ray sources observed from Tenma." In: PASJ 36, pp. 741–759.

Motta, S. E. et al. (May 2021). "Observations of a radio-bright, X-ray obscured GRS 1915+105". In: MNRAS 503.1, pp. 152–161. DOI: 10.1093/mnras/stab511. arXiv: 2101.01187 [astro-ph.HE].

Murata, K. L. et al. (May 2019). "Near-infrared variations of GRS 1915+105 in an unusual state". In: *The Astronomer's Telegram* 12769, p. 1.

Narayan, Ramesh and Insu Yi (June 1994). "Advection-dominated Accretion: A Self-similar Solution". In: ApJ 428, p. L13. DOI: 10.1086/187381. arXiv: astro-ph/9403052 [astro-ph].

Negoro, H. et al. (July 2018). "MAXI/GSC observes GRS 1915+105 in the X-ray faintest state in the last 22 years". In: *The Astronomer's Telegram* 11828, p. 1.

Neil, Ethan T., Charles D. Bailyn, and Bethany E. Cobb (Mar. 2007). "Infrared Monitoring of the Microquasar GRS 1915+105: Detection of Orbital and Superhump Signatures". In: ApJ 657.1, pp. 409–414. DOI: 10.1086/510287. arXiv: astro-ph/0610480 [astro-ph].

Neilsen, J. et al. (May 2016). "A Super-Eddington, Compton-thick Wind in GRO J1655-40?" In: ApJ 822.1, 20, p. 20. DOI: 10.3847/0004-637X/822/1/20. arXiv: 1603.04070 [astro-ph.HE].

Neilsen, J. et al. (Jan. 2021). "A NICER View of a Highly Absorbed Flare in GRS 1915+105". In: *American Astronomical Society Meeting Abstracts*. Vol. 53. American Astronomical Society Meeting Abstracts, 427.05, p. 427.05.

Ponti, G. et al. (May 2012). "Ubiquitous equatorial accretion disc winds in black hole soft states". In: MNRAS 422.1, pp. L11–L15. DOI: 10.1111/j.1745-3933.2012.01224.x. arXiv: 1201.4172 [astro-ph.HE].

Pooley, G. G. and R. P. Fender (Dec. 1997). "The variable radio emission from GRS 1915+=105". In: MNRAS 292.4, pp. 925–933. DOI: 10.1093/mnras/292.4.925. arXiv: astro-ph/9708171 [astro-ph].

Predehl, P. and J. H. M. M. Schmitt (Jan. 1995). "X-raying the interstellar medium: ROSAT observations of dust scattering halos." In: A&A 500, pp. 459–475.

Pringle, J. E. (Jan. 1981). "Accretion discs in astrophysics". In: ARA&A 19, pp. 137–162. DOI: 10.1146/annurev.aa.19.090181.001033.

Proga, Daniel (Mar. 2003). "Numerical Simulations of Mass Outflows Driven from Accretion Disks by Radiation and Magnetic Forces". In: ApJ 585.1, pp. 406–417. DOI: 10.1086/345897. arXiv: astro-ph/0210642 [astro-ph].

Punsly, Brian and Jérôme Rodriguez (May 2016). "A Temporal Analysis Indicates a Mildly Relativistic Compact Jet in GRS 1915+105". In: ApJ 823.1, 54, p. 54. DOI: 10.3847/0004-637X/823/1/54. arXiv: 1603.07675 [astro-ph.HE].

Rees, M. J. (July 1966). "Appearance of Relativistically Expanding Radio Sources". In: Nature 211.5048, pp. 468–470. DOI: 10.1038/211468a0.

Reid, M. J. et al. (Nov. 2014). "A Parallax Distance to the Microquasar GRS 1915+105 and a Revised Estimate of its Black Hole Mass". In: ApJ 796.1, 2, p. 2. DOI: 10.1088/0004-637X/796/1/2. arXiv: 1409.2453 [astro-ph.GA].

Rodriguez, J. et al. (Mar. 2008). "2 Years of INTEGRAL Monitoring of GRS 1915+105. I. Multiwavelength Coverage with INTEGRAL, RXTE, and the Ryle Radio Telescope". In: ApJ 675.2, pp. 1436–1448. DOI: 10.1086/527369. arXiv: 0712.0456 [astro-ph].

Rothstein, David M., Stephen S. Eikenberry, and Keith Matthews (June 2005). "Observations of Rapid Disk-Jet Interaction in the Microquasar GRS 1915+105". In: ApJ 626.2, pp. 991–1005. DOI: 10.1086/429217. arXiv: astro-ph/0501624 [astro-ph].

Russell, David (Jan. 2018). "Optical/Infrared Polarised Emission in X-ray Binaries". In: *Galaxies* 6.1, p. 3. DOI: 10.3390/galaxies6010003. arXiv: 1801.06713 [astro-ph.HE].

Sakimoto, Kiyoshi et al. (Sept. 2012). "An optical and near-infrared multipurpose instrument HONIR". In: *Ground-based and Airborne Instrumentation for Astronomy IV*. Ed. by Ian S. McLean, Suzanne K. Ramsay, and Hideki Takami. Vol. 8446.

Society of Photo-Optical Instrumentation Engineers (SPIE) Conference Series, 844673, p. 844673. DOI: 10.1117/12.926425.

Shah, Zahir et al. (June 2021). "Unveiling the broad-band spectral and temporal properties of PKS 0903-57 during its brightest flare". In: MNRAS 504.1, pp. 416–427. DOI: 10.1093/mnras/stab834. arXiv: 2103.13657 [astro-ph.HE].

Shakura, N. I. and R. A. Sunyaev (June 1973). "Reprint of 1973A&A....24..337S. Black holes in binary systems. Observational appearance." In: A&A 500, pp. 33–51.

Shidatsu, M., C. Done, and Y. Ueda (June 2016). "An Optically Thick Disk Wind in GRO J1655-40?" In: ApJ 823.2, 159, p. 159. DOI: 10.3847/0004-637X/823/2/159. arXiv: 1604.04346 [astro-ph.HE].

Steeghs, D. et al. (May 2013). "The Not-so-massive Black Hole in the Microquasar GRS1915+105". In: ApJ 768.2, 185, p. 185. DOI: 10.1088/0004-637X/768/2/185. arXiv: 1304.1808 [astro-ph.HE].

Trushkin, S. A. et al. (June 2019). "RATAN-600 multi-frequency measurements of GRS1915+105". In: *The Astronomer's Telegram* 12855, p. 1.

— (Feb. 2020). "Most bright radio flare of GRS 1915+105 for last decade". In: *The Astronomer's Telegram* 13442, p. 1.

Ueda, Y. et al. (June 2002). "Study of the Largest Multiwavelength Campaign of the Microquasar GRS 1915+105". In: ApJ 571.2, pp. 918–935. DOI: 10.1086/340061. arXiv: astro-ph/0202154 [astro-ph].

Ueda, Yoshihiro, Kazutaka Yamaoka, and Ronald Remillard (Apr. 2009). "GRS 1915+105 in "Soft State": Nature of Accretion Disk Wind and Origin of X-ray Emission". In: ApJ 695.2, pp. 888–899. DOI: 10.1088/0004-637X/695/2/888. arXiv: 0901.1982 [astro-ph.HE].

Vadawale, S. V. et al. (Nov. 2003). "On the Origin of the Various Types of Radio Emission in GRS 1915+105". In: ApJ 597.2, pp. 1023–1035. DOI: 10.1086/378672. arXiv: astro-ph/0308096 [astro-ph].

van der Laan, H. (Sept. 1966). "A Model for Variable Extragalactic Radio Sources". In: Nature 211.5054, pp. 1131–1133. DOI: 10.1038/2111131a0.

Vishal, Joshi, Banerjee, and K. P. Dipankar (May 2019). "Near-infrared observations of GRS 1915+105 in an unusual state with 1.2m Mount Abu telescope". In: *The Astronomer's Telegram* 12806, p. 1.

Wilson, C. A. et al. (Aug. 1994). "X-Ray Nova in Scorpius". In: IAU Circ. 6056, p. 2.

Yadav, J. S. (July 2006). "Connection between the Accretion Disk and Superluminal Radio Jets and the Role of the Radio Plateau State in GRS 1915+105". In: ApJ 646.1, pp. 385–393. DOI: 10.1086/504787. arXiv: astro-ph/0604096 [astro-ph].

Zhang, S. N. et al. (Aug. 1994). "X-Ray Nova in Scorpius". In: IAU Circ. 6046, p. 1.

Ziółkowski, Janusz and Andrzej A. Zdziarski (Aug. 2017). "The mass, luminosity and mass-loss rate of the donor of the V1487 Aql/GRS 1915+105 binary system". In: MNRAS 469.3, pp. 3315–3321. DOI: 10.1093/mnras/stx1084. arXiv: 1702.07907 [astro-ph.HE].